![Técnico Lisboa logo]

Block copolymer micelles for targeted delivery of anticancer drugs and radioisotopes

Joana Filipa da Silva Santos

Thesis to obtain the Master of Science Degree in

Chemical Engineering

Supervisors :   Doctor Célia Maria da Cruz Fernandes
Doctor Francisco França Alcântara Conceição Silva

Examination Committee

Chairperson: Prof. José Nuno Aguiar Canongia Lopes
Supervisor: Doctor Francisco França Alcântara Conceição Silva
Members of the Committee: Doctor João Domingos Galamba Correia
Prof. Vasco Daniel Bigas Bonifácio

November 2021

The work presented in this thesis was performed at the Radiopharmaceutical Sciences Group of the Center for Nuclear Sciences and Technologies (C^2TN) of Instituto Superior Técnico (IST) (Lisbon, Portugal), under the supervision of Doctor Célia Fernandes and Doctor Francisco Silva.

Acknowledgments

I would like to thank to my supervisors, Doctor Célia Fernandes and Doctor Francisco Silva for the incredible support given during my thesis. Thank you for being always present to answer my questions, for all the explanations and for always having an encouraging word.

To everyone at the Radiopharmaceutical Sciences Group at C^2TN, thank you for welcoming me and for being always available to help.

To Doctor Fernanda Marques, for teaching me about cell assays and for taking the time to answer my questions.

To my laboratory colleagues, for being there to share worries and laughs and to help keeping me calm during the more stressful days.

To my high school friends, for being there for me every time, in person or at the distance of a message or Zoom call. Thank you for the days we are together, when I can forget about all my worries. I am grateful for all the laughs and memories we shared during all of these years together and hope we will stay together to share many more moments of our lives.

To my friends from IST, thank you for sharing these 5 years with me. For all the days and nights spent studying together, even when we would do everything but study. For your patience dealing with all of my panic and for making an effort to get to know me through my social anxiety. You were an essential part of my life during these years and were able to make my days happier with all of your inappropriate jokes and even when you were always making fun of me. Thank you for helping me keep my sanity throughout this years of stress and I hope we will stay connected for many more years.

To my family, for always supporting me throughout my life. To my grandparents, who I know would be proud if they could see what I have accomplished. To my older sister, for all the advises and help. To my mum, for the unconditional love and for always encouraging me to do better. To my stepmother, for always accepting me and my sister as true daughters and for always being present during my life. To my dad, for the unconditional love and support and for always believing in me. To the rest of my family, thank you for always being there for me.

I want to dedicate this thesis to all of you who were a part of my life and helped me during this process.

Resumo

O cancro do ovário mantém-se um desafio, apesar dos avanços na sua deteção e tratamento. Estudos anteriores mostraram atividade promissora do complexo de ouro $[Au(cdc)_2]^-$ (cdc = cianoditioimido carbonato) em células deste cancro. No entanto, a sua fraca solubilidade em água representa uma desvantagem para desenvolvimentos futuros. Para ultrapassar isto, este pode ser encapsulado em micelas poliméricas, podendo ser decoradas com ligandos dirigidos aos recetores do folato, sobreexpressos nas células do cancro do ovário, aumentando a especificidade e seletividade. Neste contexto, micelas carregadas com $[Au(cdc)_2]^-$ funcionalizadas e não-funcionalizadas com ácido fólico foram sintetizadas, caracterizadas e realizou-se uma avaliação biológica preliminar. Além disso, a síntese de congéneres radiomarcados com ^{111}In-oxina também foi realizada com o intuito de explorar estas plataformas para uma aplicação teranóstica.

As micelas foram obtidas com diâmetro hidrodinâmico menor que 200 nm, potencial zeta indicativo de alta estabilidade e teor de carregamento elevado. Estudos de libertação *in vitro* mostraram que a libertação do complexo é ligeiramente mais rápida para pH menor, tendo as micelas funcionalizadas mostrado uma libertação mais controlada. Estudos preliminares de atividade antiproliferativa mostraram que estas micelas apresentam atividade significativa em células A2780, A2780cisR e OVCAR3 do cancro do ovário, comparável com o complexo livre. As micelas radiomarcadas foram obtidas com elevada eficiência ($>$90%) e retenção de ^{111}In-oxina acima dos 80% em meio fisiológico até 72 h a 37°C.

A citotoxicidade significativa e elevada estabilidade in vitro destas micelas sugerem que estas plataformas podem ser promissoras para uma potencial aplicação na teranóstica do cancro do ovário.

Palavras-chave: micelas poliméricas, complexo de ouro, veiculação de fármacos, terapia dirigida, micelas radiomarcadas

Abstract

Ovarian cancer remains a challenge despite significant advances in detection and treatment. Previous studies showed promising activity of the gold complex $[Au(cdc)_2]^-$ (cdc = cyanodithioimido carbonate) in ovarian cancer cells. However, its poor water solubility presents a drawback for further developments. To overcome this, it can be encapsulated in block copolymer micelles (BCMs), which can be decorated with ligands to target folate receptors, overexpressed in ovarian cancer cells, increasing the specificity and selectivity. Within this context, BCMs loaded with the complex $[Au(cdc)_2]^-$ functionalized and non-functionalized with folic acid were synthesized, characterized and a preliminary biological evaluation was performed. Moreover, the synthesis of radiolabeled counterparts with ^{111}In-oxine was also performed, aiming to explore these platforms for an application in theranostics.

The BCMs were obtained with hydrodynamic diameters below 200 nm, zeta potential values suggesting high stability and high loading content. *In vitro* release studies showed that the release of the complex is slightly faster with the decrease of the pH of the medium, with the functionalized micelles showing a more controlled release. Preliminary antiproliferative studies showed that these BCMs display significant activity towards A2780, A2780cisR and OVCAR3 ovarian cancer cells, comparable to the free gold complex. The radiolabeled BCMs were obtained with high yield (>90%) and a retention of ^{111}In-oxine above 80% in physiological media up to 72 h at 37°C.

The significant cytotoxicity and suitable *in vitro* stability of these BCMs suggest that these platforms could constitute promising strategies for a potential application in ovarian cancer theranostics.

Keywords: block copolymer micelles, gold complex, drug delivery, targeted therapy, radiolabeled micelles

x

Contents

List of Tables

List of Figures

Abbreviations

ACN Acetonitrile

$BCMs$ Block Copolymer Micelles

CDC Cyanodithiomido carbonate

CMC Critical Micellar Concentration

CT Computed Tomography

D_h Hydrodynamic Diameter

DCC Dicyclohexylcarbodiimide

DCM Dichloromethane

DLS Dynamic Light Scattering

$DMSO$ Dimethyl Sulfoxide

DNA Deoxyribonucleic Acid

$EGFR$ Epidermal Growth Factor Receptor

EPR Enhanced Permeability and Retention

FA Folic Acid

FBS Fetal Bovine Serum

FDA Food and Drug Administration

$FR\alpha$ Folate receptor α

$HPLC$ High Performance Liquid Chromatography

$ITLC - SG$ Instant Thin Layer Chromatography - Silica Gel

LC Loading Content

LDV Laser Doppler Velocimetry

LE Loading Efficiency

LET Linear Energy Transfer

MRI Magnetic Resonance Imaging

$NETs$ Neuroendocrine Tumors

NHS N-hydroxysuccinimide

$NIBS$ Non-invasive Back Scatter

NMR Nuclear Magnetic Resonance Spectroscopy

$PARP$ Poly (ADP-Ribose) Polymerase

PBS Phosphate Buffer Saline

PCL Polycaprolactone

PDI Polydispersity Index

PEG Polyethylene Glycol

PET Positron Emission Tomography

PTX Paclitaxel

RCP Radiochemical Purity

RES Reticuloendothelial System

ROS Reactive Oxygen Species

RT Room Temperature

$SPECT$ Single-Photon Emission Computed Tomography

TBA Tetrabutyl Ammonium

TFA Trifluoroacetic Acid

TPP Tetraphenylphosphonium

$TrxR$ Thioredoxin Reductases

$VEGF$ Vascular Endothelial Growth Factor

Chapter 1

Introduction

1.1 Motivation

Cancer is one of the leading causes of death in the world. In fact, in the majority of countries, cancer is the main responsible for premature deaths, with numbers rising over the years. Ovarian cancer, in particular, despite not being one of the most prevalent, is the gynecological cancer with the highest mortality rate due to late diagnosis [1].

Current treatments include surgical resection of tumors, chemotherapy and radiotherapy. Chemotherapy is a treatment that commonly displays undesirable toxic side effects, due to the lack of specificity. Moreover, many cancers develop resistance to the anticancer drugs used in chemotherapy, making it relevant to study new drugs, preferably with different mechanisms of action [2, 3]. Also, the unfavorable biodistribution of the drugs, short circulation half-life and poor water solubility constitute limitations to the therapeutic efficacy of this treatment [2].

To overcome these limitations, several drug delivery systems have been studied, such as micelles, allowing the delivery of anticancer drugs to targeted tumor sites, with less associated toxicity [4].

1.2 Topic Overview

A monoanionic gold (III) bisdithiolate complex, $[Au(cdc)_2]^-$ (where cdc = cyanodithiomido carbonate) had been previously studied and exhibited significant antiproliferative activity in ovarian cancer cell lines, both sensitive and resistant to cisplatin, with low toxicity [5]. This complex's mechanism of action differs from that of commonly used anticancer drugs, being a promising way to address the problem of drug resistance. However, this complex has poor water solubility, presenting a limitation to

its efficacy *in vivo*. A way to overcome this issue is by encapsulating the complex in block copolymer micelles (BCMs).

BCMs are constituted by amphiphilic copolymers and self-assemble in aqueous medium, having a hydrophobic core surrounded by a hydrophilic corona. Due to their structural arrangement, it is possible to encapsulate hydrophobic drugs in their core, increasing the solubility of the drugs and therefore the half-life circulation in the blood [6, 7]. Furthermore, the corona of the micelles can be decorated with targeting ligands, to increase the specificity and selectivity and reduce toxicity, allowing a targeted delivery of anticancer drugs and radioisotopes [8]. In this case, the gold complex will be encapsulated in the BCMs to tackle the low solubility problem and the corona will be functionalized with folic acid, which has high affinity to the folate receptor, which is overexpressed in several epithelial tumors, namely ovarian cancer, allowing to target this type of tumors and therefore increase therapeutic efficacy [9]. With this approach, the folic acid present in the micelles binds to the folate receptor, which is overexpressed in ovarian cancer cells, and is internalized in the cell by receptor-mediated endocytosis [10, 11].

For a theranostic approach, radionuclides can also be incorporated into the micelles, along with the anticancer drugs, allowing for an image-guided drug delivery system. These radionuclides can be either conjugated to the outer shell of the BCMs or encapsulated in the core [12–14]. In this thesis, the radionuclide was entrapped in the core of the micelles by forming a hydrophobic complex with 8-hydroxyquinoline, exploiting their ability to encapsulate hydrophobic compounds. With this technique, it is possible to indirectly extrapolate the biodistribution of the drug without having to chemically modify the structure of the BCMs.

Figure 1.1 presents a scheme of the thesis overview.
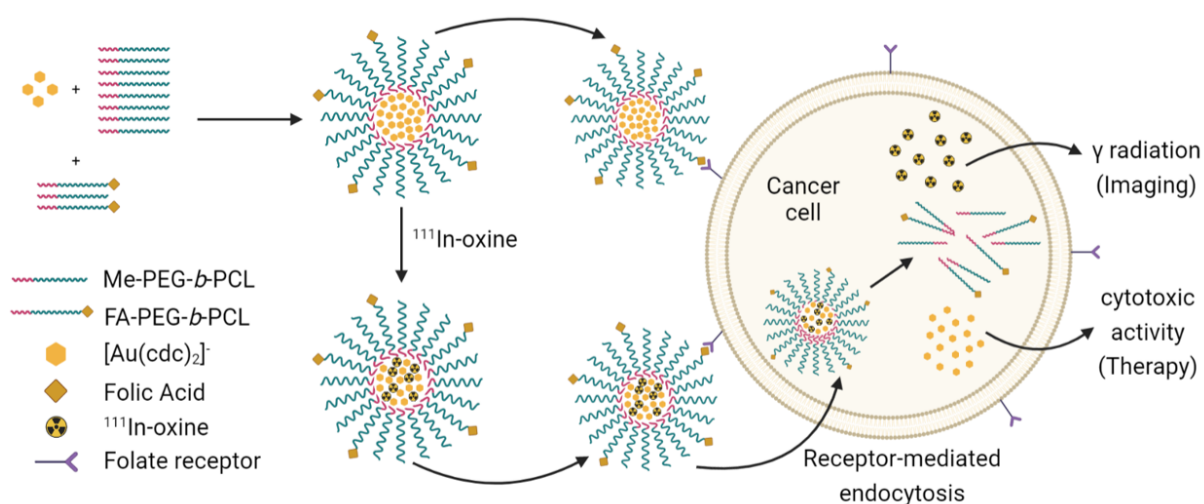
Figure 1.1: Scheme of the thesis overview.

1.3 Thesis Aim

The aim of this thesis was to encapsulate a cytotoxic gold complex ($[Au(cdc)_2]^-$) in the core of block copolymer micelles to improve its solubility, increasing the circulation half-life in the blood and providing higher selectivity, with less side effects, through the enhanced permeability and retention (EPR) effect, while using an active targeting approach by functionalizing them with folic acid to target the folate receptor, aiming to increase its therapeutic efficacy. These platforms were further explored for simultaneous delivery of cytotoxic drugs and radioisotopes (^{111}In), for cancer theranostics.

In this work, the preparation and characterization of BCMs loaded with $[Au(cdc)_2]^-$, using the copolymer PEG-b-PCL, functionalized or not with folic acid is reported. Furthermore, the *in vitro* $[Au(cdc)_2]^-$ release from the BCMs was evaluated in physiological conditions and in slightly acidic conditions. Also, the antiproliferative activity was evaluated in selected ovarian cancer cell lines. Finally, the radiolabeling of the BCMs with the hydrophobic complex ^{111}In-oxine and *in vitro* stability studies are also presented.

1.4 Thesis Outline

This thesis is divided in five chapters. The first chapter gives a brief introduction to the topic of this thesis and presents the overall aim. The second chapter contains the background, with the theoretical aspects of the subjects addressed in the thesis. The third chapter presents the experimental procedures. The fourth chapter shows the results and discussion of the work performed. The fifth chapter contains the overall conclusions and future perspectives regarding this work.

Chapter 2

Background

2.1 Ovarian cancer

Ovarian cancer is the third most common gynecologic cancer in the world, having the highest mortality rate. In fact, despite having a significantly lower incidence than breast cancer, it is three times more lethal. The delayed onset of symptoms leads to a late stage diagnosis, with only 25% of women being diagnosed in stage I of the disease, having an overall 5-year survival rate of above 90%, value that decreases to 10% when diagnosed in an advanced stage [1, 15].

The current treatment used for advanced ovarian cancers is the surgical resection of the tumor, followed by chemotherapy with platinum-based compounds, such as cisplatin, and taxanes, namely paclitaxel (PTX), however, since a majority of patients ultimately relapse, the repetition of chemotherapy can lead to drug resistance [2, 3].

Additionally, chemotherapy treatments often incur unwanted side effects, due to lack of specificity and associated toxicity. Taxane chemotherapy agents present poor pharmacokinetics and have significant hydrophobicity. In order to improve drug efficacy, while minimizing the impact on healthy tissues, targeted drug delivery systems, such as micelles, present a promising pathway for improving the solubility and pharmacokinetic profile of the drugs, while reducing the unwanted toxicity [2, 16].

Aiming to increase selectivity, targeted therapy has been explored, with ovarian cancer presenting several possible targets, such as folate receptor α (FRα), vascular endothelial growth factor (VEGF) receptor, epidermal growth factor receptor (EGFR), poly (ADP-ribose) polymerase (PARP), among others [9, 17]. One of the most commonly used targets for imaging and therapy of ovarian cancer is the FRα, a folate-binding protein that is overexpressed in several tumors of epithelial origin, with approximately 80% of epithelial ovarian tumors overexpressing FRα, while normal ovarian epithelium presents negligible expression [9].

2.2 Gold complexes for medical applications

The increasing number of individuals affected by cancer and multi-resistant infections, along with the side effects associated with chemotherapeutic drugs and the emergence of drug resistance to anticancer drugs, has led to an increased interest in the research of new compounds with both antimicrobial and anticancer properties [18].

Gold complexes have shown to be promising for this purpose, with auranofin being the most significant. Auranofin is a gold(I) complex approved for the treatment of rheumatoid arthritis, however, with the emergence of new drugs that are more effective and present fewer side effects, its use for this disease has become extremely rare. Nonetheless, this drug has shown potential for the treatment of several other diseases, such as different types of tumors, including leukemia and ovarian cancer, with Phase II Food and Drug Administration (FDA) approved clinical trials currently active [19–21]. Moreover, when investigating potential new gold-based drugs, auranofin is often used as a reference compound [22].

More recently, several gold (I/III) complexes have shown significant antitumor activity. These gold complexes were found to exhibit substantial antiproliferative activity against cancer cells *in vitro*, at low concentrations. Furthermore, some gold (I) complexes demonstrated to be selectively cytotoxic for tumor cell lines and several exhibited numerous antitumor mechanisms, such as thioredoxin reductases (TrxR) inhibition, Deoxyribonucleic Acid (DNA) damage, accumulation of reactive oxygen species (ROS), apoptosis induction, among others [23].

The mechanism of action of gold complexes is different from cisplatin or its derivatives, which are one of the most commonly used chemotherapeutic drugs. While cisplatin and its derivatives target DNA, gold complexes usually target enzymes, particularly those containing thiols, due to the strong binding affinity of the gold ions to thiols. Several enzymes and other biological substrats that contain thiol groups are overexpressed in cancer cells, such as TrxR, glutatione reductases and cysteine. The inhibition of the enzymes leads to a significant increase in ROS and, consequently, to apoptosis. The differences in the mechanisms of cisplatin and gold-based chemotherapeutics makes most gold complexes effective against cisplatin-resistant cancer cells, representing a promising approach in solving the problem of drug resistance of cancer cells to commonly used drugs [24].

A recent study addressed the antimicrobial and antitumor activity of different monoanionic gold (III) bisdithiolate complexes, using auranofin and cisplatin as reference [5]. The gold complexes TBA[Au(mnt)$_2$] (where mnt = 1,1-dicyanoethylene-2,2'-dithiolate), TBA[Au(*i*-mnt)$_2$] (where i-mnt = 2,2-dicyanoethylene-1,1-dithiolate), TBA[Au(cdc)$_2$] (where cdc = cyanodithioimido carbonate) and TPP[Au(qdt)$_2$] (where qdt = quinoxaline-2,3-dithiolate) were prepared as tetrabutyl ammonium (TBA) and tetraphenylphosphonium (TPP) salts. The molecular structures of the complexes and of the reference drugs auranofin and cisplatin are presented in Figure 2.1.
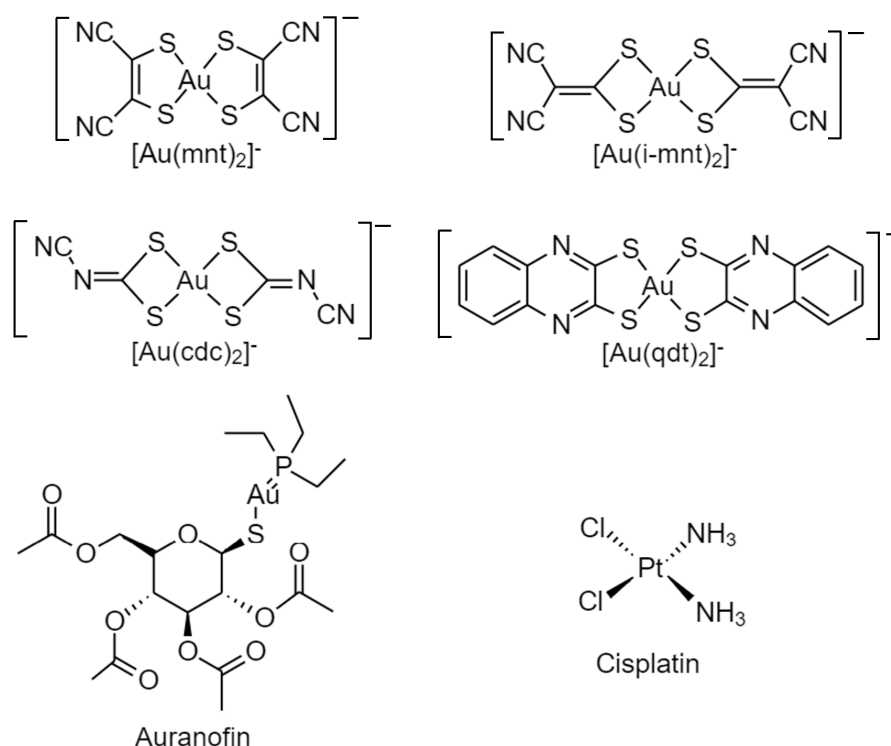
Figure 2.1: Molecular structure of [Au(mnt)$_2$]$^-$ (where mnt = 1,1-dicyanoethylene-2,2'-dithiolate), [Au(*i*-mnt)$_2$]$^-$ (where *i*-mnt = 2,2-dicyanoethylene-1,1-dithiolate), [Au(cdc)$_2$]$^-$ (where cdc = cyanodithioimido carbonate), [Au(qdt)$_2$]$^-$ (where qdt = quinoxaline-2,3-dithiolate), auranofin and cisplatin. Adapted from [5].

The cytotoxicity of the complexes and of the reference compounds was assessed in the cisplatin in the cisplatin-sensitive A2780 and in the cisplatin-resistant A2780cisR ovarian cancer cell lines and in the fibroblast normal cell line V79. Table 2.1 presents a summary of the IC$_{50}$ values (the concentration of complex required for 50% inhibition) obtained [5].

Table 2.1: IC$_{50}$ values (μM) determined after 48 h incubation for four gold complexes synthesized at C^{2}TN/IST and reference drugs auranofin and cisplatin in the ovarian cancer cells A2780 and A2780cisR and the normal V79 fibroblasts. Results are shown as the mean $\pm$ SD of two independent experiments done with six replicates. [5]

Compounds	A2780	A2780cisR	V79	SI
TBA[Au(mnt)$_2$]	4.4 $\pm$ 1.3	5.5 $\pm$ 1.5	26 $\pm$ 4.8	6.0
TBA[Au(*i*-mnt)$_2$]	1.5 $\pm$ 0.5	2.3 $\pm$ 1.0	2.4 $\pm$ 0.7	1.6
TBA[Au(cdc)$_2$]	0.9 $\pm$ 0.2	1.7 $\pm$ 0.5	3.4 $\pm$ 1.0	3.8
TPP[Au(qdt)$_2$]	1.2 $\pm$ 0.3	1.3 $\pm$ 0.4	5.3 $\pm$ 1.1	4.4
Auranofin	0.4 $\pm$ 0.3	0.5 $\pm$ 0.17	0.7 $\pm$ 0.3	1.5
Cisplatin	3.6 $\pm$ 1.3	36 $\pm$ 13	6.7 $\pm$ 2.7	1.9

[a] SI = the selectivity index calculated as IC$_{50}$ (V79)/IC$_{50}$ (A2780).

In this thesis, the gold complex used was TBA[Au(cdc)$_2$]. As shown in Table 2.1, TBA[Au(cdc)$_2$]

presented one of the lowest IC_{50} values in the ovarian cancer cell lines. Also, this complex showed significantly higher selectivity than the reference drugs, while auranofin displayed the highest toxicity towards the normal cell line, suggesting that these new gold complexes could present advantages when compared with the reference drug auranofin. Furthermore, although presenting similar toxicity to cisplatin in the fibroblast normal cell line, it is important to note that in the cisplatin-resistant cell line, the IC_{50} values of these gold complexes were significantly lower, suggesting less cross-resistance [5].

The stability of the complexes was evaluated in solution by UV-Vis spectroscopy, with results indicating that TBA[Au(cdc)$_2$] is the most stable complex of the four studied, supporting the results obtained by cyclic voltammetry, which indicated that this complex was the most redox-stable [5].

Despite some promising results *in vitro*, this is an area with great potential for growth, with very few studies regarding the cytotoxic activity of gold complexes *in vivo*. Moreover, the mechanism of action of most of these complexes is not yet fully understood, presenting an opportunity for further investigation.

Furthermore, similarly to other chemotherapeutic drugs, these gold complexes also present poor water solubility, which could present a limitation to their application *in vivo*. To address this issue, nanoplatforms present a promising pathway for the increase of the solubility of these drugs and the subsequently increase of their circulation half-life in the blood [4].

2.3   Nanomedicine

Over the years there has been a growing interest in new and more efficient drug delivery systems, particularly for cancer therapy. Several issues have been identified in conventional antitumor therapeutics, one of the most important being the unfavorable biodistribution of the drugs. After intravenous administration, the drugs are rapidly cleared from circulation, causing a reduction of the dose that actually reaches the tumor. Furthermore, in order for the drug to exhibit its therapeutic effect, it has to remain in the tumor site long enough to perform its desired function, which may not happen due to rapid clearance. In addition to rapid degradation, the lack of specificity of the drugs, their poor water solubility, among other factors, causes the pharmaceuticals to reach undesired tissues, causing potential side effects [25, 26].

The development of drug delivery systems that can target specific tumor sites, thus decreasing toxicity, presents a promising approach for the improvement of cancer therapeutics. The application of nanoparticles for drug delivery has been widely explored, aiming to improve the biodistribution and site-specific delivery of the pharmaceuticals [25]. Several types of nanomedicines have been studied, being able to selectively deliver the drugs to tumors, increasing their accumulation in targeted tissues and reducing toxicity and can be divided in three classes: polymeric nanoparticles, inorganic nanoparticles and lipid-based nanoparticles (Figure 2.2) [4].
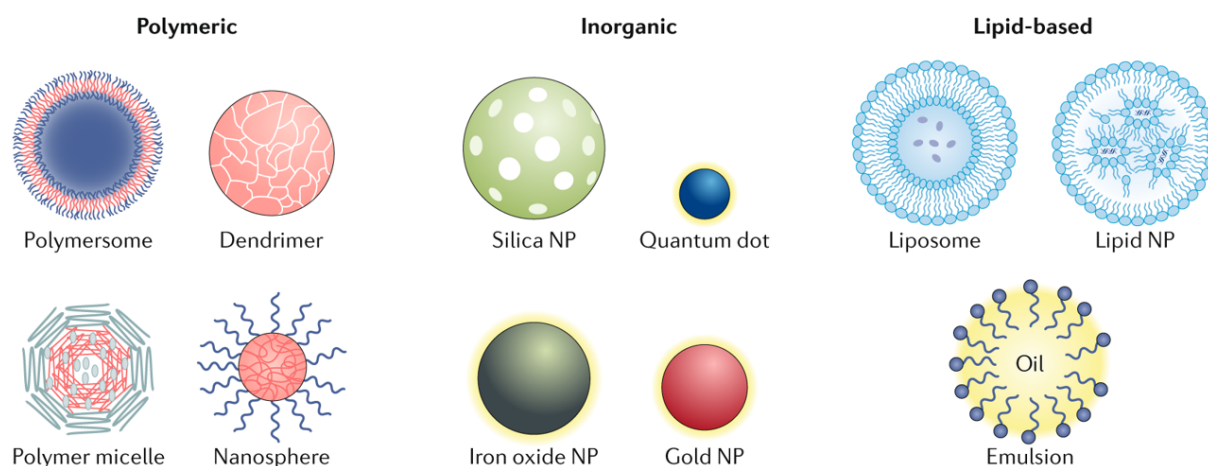
Figure 2.2: Different types of nanoparticles [4].

When using these nanoparticles, it is desirable that they maintain their stability in the blood, avoiding leakage and degradation of the loaded drugs in the blood and in the cells of the reticuloendothelial system (RES), being extravasated selectively in the tumor site. This is possible due to the relatively large size of the nanomedicines, which presents further advantages, such as the impediment of rapid renal clearance of the drugs, prolonging their circulation half-life. This can also be accomplished by shielding the surface of nanomedicines with biocompatible materials, for example, polyethylene glycol (PEG), in order to increase the solubility and plasma stability of proteins [27].

Some of the characteristics that most significantly affect the biodistribution of nanomedicines are their size and charge. They have a critical size boundary of 150 nm. Below this value, nanomedicines are more likely to accumulate in the liver, while the ones above this value are captured in the spleen. Regarding the charge, neutral or negatively charged nanomedicines present a prolonged circulation half-life, while cationic particles tend to be more cytotoxic and retained in the liver, spleen and lungs [28, 29].

The discovery of the EPR effect (Figure 2.3) represented a great breakthrough in the development of targeted antitumor therapies with nanomedicines. This effect is based on the nature of solid tumor blood vessels, that present enhanced vascular permeability, facilitating the transport and accumulation of nanometric sized particles in tumor tissues [30]. Furthermore, the poor lymphatic drainage of tumors, resultant from the collapse of lymph vessels caused by their compression by the tumor cells, also promotes the retention of the nanoparticles in tumor tissues [31]. The use of nanoparticles, as opposed to conventional small molecular drugs, provides a prolonged circulation half-life and higher selectivity, decreasing the side effects of anticancer drugs [30].
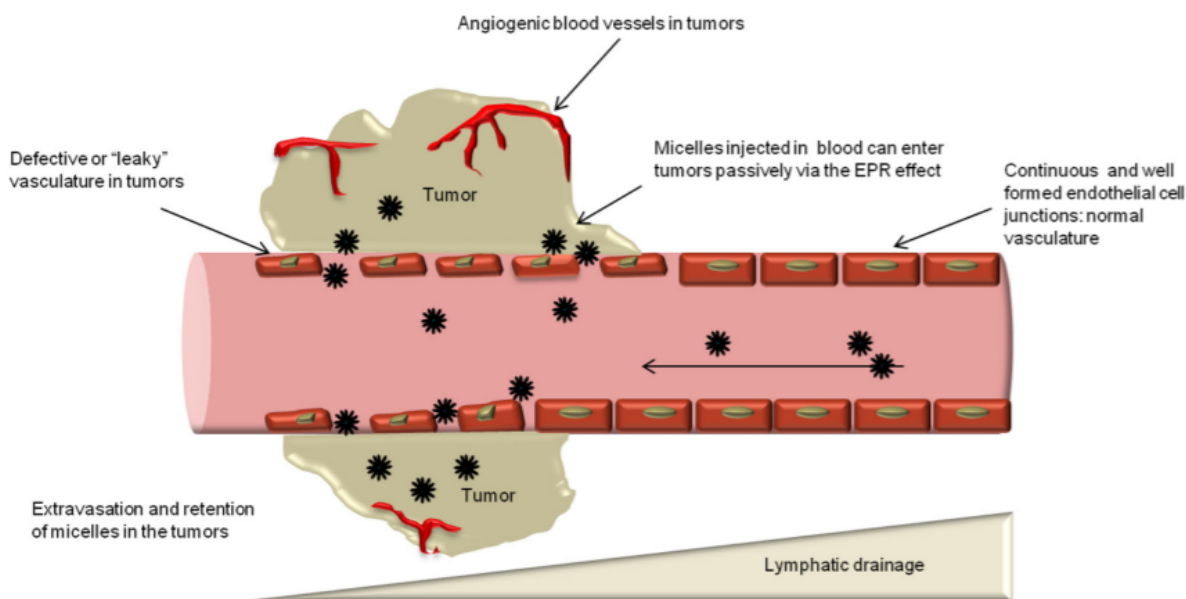
Figure 2.3: Schematic representation of the enhanced permeability and retention effect [31].

This effect, however, is affected by the pathophysiological characteristics of the tumor, such as the degree of angiogenesis and lymphangiogenesis, the density of cells and stromal components and the intratumoral pressure. It is essential that the nanomedicines have a prolonged circulation half-life and are small enough to be able to penetrate from the blood compartment into tumor tissues [32].

After the accumulation of the drugs in the targeted tissues, nanomedicines are surrounded by the cell membrane, being ingested through endocytosis, allowing the macromolecules to reach intracellular regions. Moreover, it is possible to include in the surface of nanomedicines ligand molecules that bind to specific receptors that are overexpressed in the target cells, while having negligible expression in healthy tissues, in order to improve the selectivity of anticancer drugs [33, 34].

2.3.1 Block copolymer micelles for drug delivery

The administration of anticancer drugs frequently implies the use of surfactants as drug formulation vehicles, which have low molecular weight and distribute throughout the body, generating toxicity and presenting rapid clearance [32, 35]. To maintain an effective dose in the target tissue, it is necessary to make recurrent administrations, which can cause drug resistance and chronic toxicity. The use of polymeric micelles allows for the anticancer drugs to stably circulate in the bloodstream, while being protected from the aqueous environment, selectively delivering the cargo to the tumor [32].

Micelles composed of block copolymers with amphiphilic behavior are considered promising drug delivery systems for hydrophobic anticancer agents. The amphiphilic block copolymers self-assemble in aqueous medium, with the hydrophobic blocks of the copolymer forming the core of the micelle and the hydrophilic blocks forming the corona, as shown in Figure 2.4. The uniqueness of their design allows

the incorporation of hydrophobic drugs in their core, while having the hydrophilic corona serving as a barrier to the outside aqueous environment [6, 7].
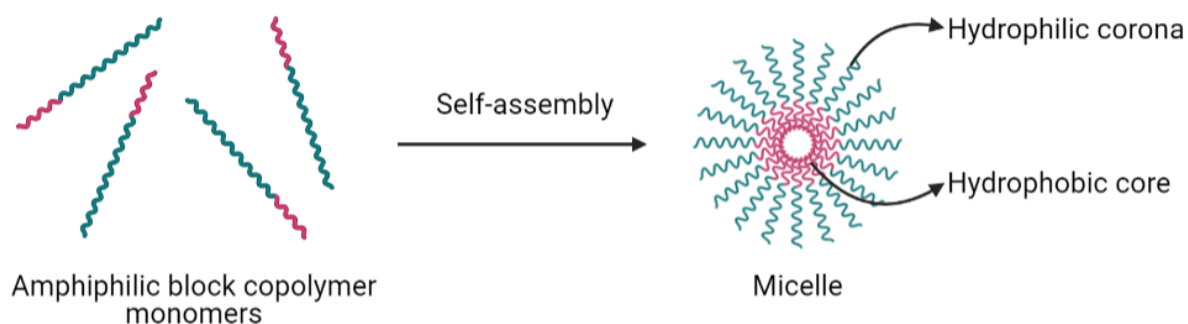
Figure 2.4: Scheme for the micellization of an amphiphilic block copolymer. Adapted from [36].

Polymeric micelles have a lower critical micellar concentration (CMC) than low molecular weight surfactant micelles, suggesting higher stability and thus, present a slower rate of dissociation. In addition, polymeric micelles are more kinetically stable, having greater stability when subjected to extreme dilution. Therefore, this type of micelles provide a longer circulation time [6, 36]. In order to avoid recognition by the RES and, therefore, increase circulation half-life, the diameter of the micelles should be ideally below 200 nm [37].

When selecting the polymers to be used it is essential to consider the safety of the materials, in addition to the structural and functional aspects. Therefore, the polymers used must be biocompatible, nontoxic and biodegradable, preventing long-term toxicity, as they can be excreted from the body by the disintegration of the polymers into its monomers [32].

The most widely used polymer for the blocks forming the shell is PEG, due to its long circulation life in the blood and low immunogenicity. The steric repulsion forces prevent the aggregation of polymeric micelles, while creating a hydrophilic protective layer to shield the charge, reducing the surface charge and charge-induced interactions in the body [38–40].

Since PEG is a non-biodegradable polymer, it is necessary to be aware of its long-term accumulation in the body. The clearance of the polymer is determined by its molecular weight; at values lower than 60 kDa it allows for renal clearance and prevent accumulation in the liver. However, there are several studies reporting problems concerning the use of PEG, such as the accelerated blood clearance phenomena in both animals and humans, consisting on a significant decrease of the circulation half-life of a second dose of PEGylated liposomes when injected a few days after the first dose and, in a scarce number of cases, allergic responses, due to specific antibody responses generated against PEG. In light of these concerns, several alternatives to PEG are being studied, mostly being biocompatible hydrophilic polymers [40, 41].

For the core forming blocks, their segregation from the aqueous milieu is the driving force for

micellization, which happens through different interactions, such as hydrophobic interaction, electrostatic interaction, metal complexation and hydrogen bonding. It is essential to maintain strong cohesive forces between the core and the drugs loaded, so that stable micellar systems can be obtained, preventing their disintegration during circulation when subjected to extreme dilution [6, 32].

The most widely used polymers for the core of the micelles are polyethers, polyesters and polyamino acids. Micelles with a polyether core have greater stability when compared with low molecular weight surfactant micelles, however, due to the relatively high CMC and low drug-polymer affinity, the stability upon injection is low. Furthermore, this type of polymer is not degraded in the body, eliciting long-term exposure. Polyesters have higher loading efficiency of hydrophobic anticancer drugs than polyethers, however, the low affinity between the polymer and the drug can cause an initial burst release of the loaded drug, which can be overcome with the crystallization of the polymer, improving the stability, decreasing the CMC and increasing the segregation of the drug in the core due to the strong interpolymer interactions. Polyamino acids allow the simple modification of side groups, therefore presenting high loading capacity and affinity with the cargo. Depending on the amino acid, it's possible for the polyamino acid to assume positive or negative charge, providing further stabilization and affinity with the drugs [32].

To facilitate the selective release of the cargo in the target tissue, it is possible to design stimuli-responsive micelles, which can take advantage of the altered conditions in tumor tissues. These signals must be endogenously present in the body and overexpressed in unhealthy tissues, so that the micelles are selectively activated in the target, or exogenous, originating from an artificial source. The endogenous stimuli are originated in the cells or tissues and can be temperature variations, pH alterations, redox potential fluctuations and ionic strength disparities. In the specific case of tumors, they present some distinctive conditions, such as an acidic pH and an elevated temperature, which can be used as stimuli. The exogenous stimuli can be done with heat, ultrasound, light irradiation and magnetic or electric fields. These two types of stimulus can be used simultaneously, in order to achieve a higher therapeutic efficacy [42].

The hydrophobic drugs can be physically incorporated in the micelles or reversibly conjugated to the core-forming segments via labile bonds. In both cases, stimuli-responsive micelles can be designed, in order to obtain a more selective drug release. For example, in the case of micelles with a polyester core, the hydrolysis of the ester bonds is enhanced in acidic pH, characteristic of tumors, leading to an accelerated drug release in this environment. When physically incorporating the drugs, *i.e.*, using the free drug in the micelle formulation, this release does not happen concurrently with the pH change, with a gradual release happening instead. By forming micelles with a copolymer conjugated with the drug, by labile bonds, without the use of the free drug, the chemical bonds between it and the polymer are stable at physiological pH but are rapidly degraded in the mildly acidic environment of tumors. Thus, leading to a quick drug release in the unhealthy tissues, decreasing drug leakage during circulation and improving the selectivity of drug release [32, 43].

A major limitation with the application of micelles in particular intracellular targets is the low

cellular uptake, mainly observed in PEGylated nanomedicines. The use of PEG allows to achieve a longer circulation time, due to the EPR effect, however, it simultaneously inhibits the internalization of nanomedicines [8].

To overcome this limitation, it is possible to decorate the surface of the micelles with bioactive ligand molecules, in order to increase cellular uptake, allowing to increase the therapeutic efficacy [8]. The efficacy of this approach is determined by different parameters, including the density of ligands, the flexibility of the ligand-micelle spacer, the binding affinities and the expression of the receptor. The binding affinities may be enhanced due to multivalent conjugation of ligands on the surface of the micelle, the receptor internalization, the biodistribution and availability of the receptor [32]. It is essential to have extensive knowledge on how the receptor expression behaves for different cancer stages, since this factor can affect the therapeutic efficiency. In some tumors, the degree of overexpression of the receptor can be related with parameters of biological aggressiveness, with cancers at an advanced stage showing a higher degree of overexpression [44].

Numerous ligands have been studied and their targeting efficiency has been confirmed, such as proteins, peptides, antibodies and aptamers (Figure 2.5) [8]. However, several studies reported that the presence of ligands in nanomedicines does not always increase the accumulation of drugs in the tumor, with this accumulation being attributed to the EPR effect. Nonetheless, ligands can be useful to overcome some biological limitations presented by the EPR effect, such as the difficulty to reach deeper tumor tissue and interaction with targeted cells after accumulation [45, 46].
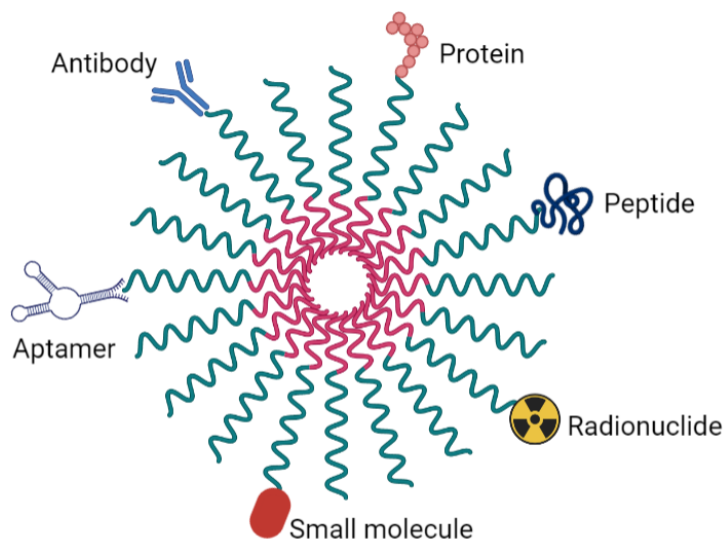
Figure 2.5: Different types of targeting ligands that can be used for targeted therapy.

Folic acid has high affinity to FRα and, therefore, can be used as a targeting ligand for imaging and therapy of ovarian cancer, minimizing the toxicity in normal tissues. Once bound to the folate receptor, folic acid and folate-linked cargos, such as chemotherapeutics, imaging agents, therapeutic radionuclides and nanoparticles, are internalized in the cell by receptor-mediated endocytosis [10, 11].

2.4 Nuclear medicine

Nuclear medicine is a medical field based on the application of radionuclides, taking advantage of the different physical properties that radioactive elements present. Nuclear medicine approaches are applied, both for therapy and imaging, in several medical specialties, such as oncology, cardiology, endocrinology and neuropsychiatry, among others, mainly in molecularly sensitive processes, since radiopharmaceuticals work on the "tracer principle", meaning that the dosing is minimal, allowing the maintenance of the biology of the system. There are still several challenges to overcome in this area, such as improving the precision of imaging and the selectivity of therapy, as well as further explore the possibility of pairing diagnostics and therapeutics [11].

Nowadays, nuclear medicine approaches for both therapy and imaging are used as standard care. The area of theranostic (i.e. combination of imaging and therapy) is in continuous growth and holds great promise for the future of nuclear medicine [47].

This medical specialty uses radiopharmaceuticals, which are a group of drugs that contain a radioactive label [48]. The radiopharmaceuticals can be divided in two groups: perfusion or first generation radiopharmaceuticals and specific or second generation radiopharmaceuticals. The perfusion radiopharmaceuticals are the most commonly used in clinical practice. These radiopharmaceuticals do not have any targeting moiety and their biodistribution is determined by blood perfusion and by the size and charge of the compound. The specific radiopharmaceuticals (Figure 2.6) have a vector molecule (e.g. peptide or antibody), which can target a specific biological target [49].
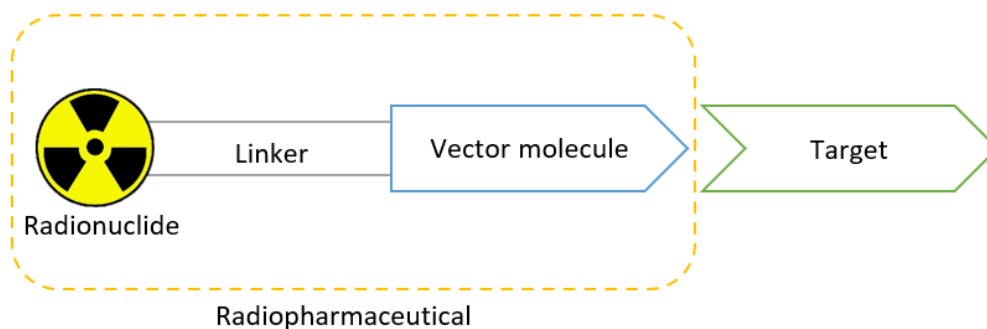
Figure 2.6: Schematic representation of a specific radiopharmaceutical.

Nuclear imaging makes use of low doses of radioactive compounds to visualize specific biological processes in the body or in certain types of tissues. This is a major advantage when compared with more conventional imaging techniques, for example, Computed Tomography (CT), because it allows better contrast, since in CT all tissues produce signal. As described by the tracer principle, radiopharmaceuticals can be used in sub-nanomolar doses, not interfering with the biochemistry of the system, while providing images with high-quality, while in CT and Magnetic Resonance Imaging (MRI), the mass dose of contrast agents can influence the system [11].

Radionuclides that decay with emission of γ photons or β^+ particles are best suited for the development of radiopharmaceuticals aiming at diagnosis, either by Single Photon Emission Computed Tomography (SPECT) or Positron Emission Tomography (PET). These nuclear imaging techniques present several advantages, such as a higher specific activity and detection sensitivity, when compared with CT and MRI, as well as the fact that it can be quantified, allowing an earlier detection and a more accurate estimation of disease staging. Nonetheless, it also has its disadvantages, like having a poorer resolution, when compared with CT and MRI, and the fact that it delivers radiation doses to the patient, even though at a low level [11, 50]. Another disadvantage of nuclear imaging modalities is the fact that the anatomic information provided is limited. This can be overcome with multimodality devices such as PET-CT and SPECT-CT that provide anatomical information in conjunction with functional molecular information [50, 51].

Table 2.2 presents examples of radionuclides used for imaging.

Table 2.2: Examples of radionuclides for imaging application [52].

Radionuclide	Emission type	Half-Life	Application
^{99m}Tc	γ	6.0 h	SPECT
^{111}In	γ	67.9 h	SPECT
^{67}Ga	γ	78.26 h	SPECT
^{123}I	γ	13.3 h	SPECT
^{18}F	β^+	110 min	PET
^{68}Ga	β^+	67.6 min	PET
^{62}Cu	β^+	9.8 min	PET
^{86}Y	β^+	14.7 h	PET

Radiopharmaceuticals can also be used to deliver radiation to a specific target in the body and radionuclide therapy can have significant advantages over conventional methods such as chemotherapy and external beam radiotherapy. Since radiopharmaceuticals are administered in low molecular doses, they do not generate biochemical effects off-target, as it happens with the drugs used in chemotherapy. Moreover, radiopharmaceuticals can deliver radiation with higher selectivity than in external beam radiotherapy, being able to not only target primary tumors, but also metastasis, reducing the toxic side effects to healthy tissues. However, there are still some limitations in this type of therapy, such as the toxicity to organs involved in the excretion of the administered radiopharmaceuticals and the specificity of the probe for the targeted disease [11].

To choose a radionuclide suitable for therapy, several factors must be taken into consideration, such as half-life, type of decay, linear energy transfer (LET) and particle range in tissue, so that the radiopharmaceutical is specifically developed according to the tumor being targeted. For example, for the treatment of cancers such as leukemia and lymphoma, particles with lower energy are more suitable, while for the treatment of solid tumors, particles with higher energy must be used [11, 53]. Therapeutic

radionuclides are α or β^- emitters, although interest in the therapeutic potential of Auger emitters has been increasing recently. Table 2.3 presents examples of radionuclides used for therapy.

Table 2.3: Examples of radionuclides for therapeutic application [52].

Radionuclide	Emission type	Half-Life
^{223}Ra	α	11.4 days
^{211}At	α	7.2 h
^{131}I	β^-, γ	8 days
^{177}Lu	β^-, γ	6.71 days
^{90}Y	β^-	64 h
^{188}Re	β^-, γ	16.98 h
^{125}I	Auger e$^-$	60 days
^{111}In	Auger e$^-, \gamma$	67.9 h

2.4.1 Theranostics

The term theranostics is used in nuclear medicine when diagnostic imaging and therapy are combined into the same molecule or two very similar molecules, with the aim of developing more individualized therapies. The use of theranostics not only allows to make a better selection of patients for a specific treatment by estimating the potential response of the patient to the treatment through the visualization of potential targets using molecular imaging, but also allows to monitor the therapy while it is in course [54]. The main concern when using this type of approach is toxicity, however, several studies have proven that with a rigorous selection of patients, a high treatment efficiency can be achieved with acceptable levels of toxicity [55, 56].

For theranostic purposes, it is possible to use the same radionuclide for imaging and therapy, as in the case of ^{131}I and ^{177}Lu, since they are gamma and beta emitters, or different isotopes of the same chemical element, such as ^{123}I and ^{131}I, ^{86}Y and ^{90}Y and terbium isotopes (^{152}Tb, ^{155}Tb, ^{149}Tb and ^{161}Tb).[54]

The application of theranostics in nuclear medicine started in thyroid diseases, allowing the staging and treatment of thyroid cancer and metastatic thyroid cancer by radioactive iodine therapy. More recently, several studies have been conducted to evaluate the therapeutic efficacy of this type of treatment for other tumors, such as neuroendocrine tumors (NETs) and prostate cancer [57, 58]. The clinical use of ^{177}Lu-DOTA-TATE (Lutathera®), the first radiopharmaceutical for peptide receptor radionuclide therapy, and ^{68}Ga-DOTA-TATE (NETSPOT®), its diagnostic partner, was already approved by the FDA for the treatment of somatostatin receptor positive gastroenteropancreatic neuroendocrine tumors, becoming a highly relevant theranostic pair [59–61].

Within the field of theranostics, there is nanotheranostics, which applies the same strategy, associated with nanomedicine. The application of nanoparticles as theranostic agents allows the delivery of diagnostic and therapeutic agents in a single theranostic platform, in a more controlled manner, while presenting the possibility of the conjugation with a ligand to improve targeting and, therefore, reduce possible side effects. With theranostic nanomedicine it is possible to visualize the circulation time and target site accumulation of nanoparticles, by using non-invasive methods, contributing to a better analysis of pharmacokinetics and biodistribution and, subsequently, to the development of more optimized drug delivery systems [62, 63].

The co-delivery of diagnostic and therapeutic agents in nanoparticles presents great potential for the development of personalized therapies, allowing intracellular diagnosis and therapeutic monitoring, achieving a higher efficacy and specificity of treatment than in cases where only one agent is present in the nanoparticle [62].

In the specific case of micelles, their hydrophobic core is usually loaded with cytotoxic drugs, while the hydrophilic shell is decorated with targeting moieties. For nanotheranostics, imaging agents, such as radionuclides, can be either encapsulated in their core or conjugated to the outer shell, as will be explained in more detail in Chapter 2.5 [64, 65].

2.5   Radiolabeled Micelles

When selecting the radionuclide to be used in the radiolabeling of nanoparticles, several aspects must be taken into account, such as the physical characteristics of the radionuclide, including its half-life, type of emissions, energy of radiation, daughter products, among others, as well as some biological aspects, like tissue targeting, *in vivo* stability and toxicity. Diagnostic radionuclides must be able to provide information on biodistribution and dosimetry, having typically a short half-life, however, it should be long enough so that the radiolabeled nanoparticle can reach a significant tissue accumulation before decaying. When optimizing the radiolabeling procedure, it is important to ensure that the labeling causes the least possible alterations in the structure of the nanoparticle, so that its biodistribution is not significantly altered. Moreover, the stability of the radiolabeled nanoparticles must be assured by *in vitro* experiments [66].

As explained in Chapter 2.3.1, the fact that block copolymer micelles allow the encapsulation of hydrophobic substances, increasing their solubility, along with their long circulation half-life, high stability and ability to accumulate in tumor tissues through EPR effect makes them promising drug delivery systems. In order to study the *in vivo* behavior of the nanoparticles, nuclear imaging techniques can be applied, such as PET and SPECT, allowing to non-invasively study the biodistribution and stability of the nanocarriers, with high detection sensitivity at high resolution. For this purpose, micelles are required to be labeled with appropriate radionuclides [12, 13].

Micelles radiolabeling can be done using two different approaches (Figure 2.7). The most widely used technique involves the conjugation of a chelating agent to the polymer used in the formation of the micelle, altering its shell [14, 67]. A more recently studied technique allows the encapsulation of the radionuclide in the micellar core, using a hydrophobic chelator [12, 13].
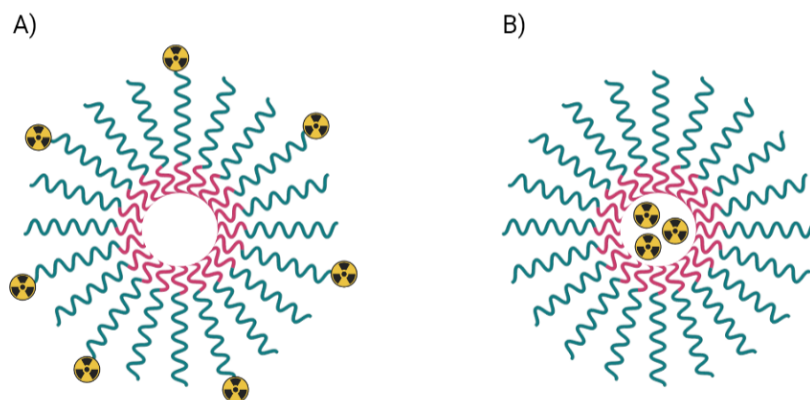
Figure 2.7: Scheme for micelles radiolabeling techniques. A) Conjugation of the radionuclide to the shell of the micelle; B) Encapsulation of the radionuclide in the micellar core.

In the first technique described, the chelating agents more commonly used are diethylene triamine pentaacetic acid (DTPA) and 1,4,7,10-tetraazacyclododecane-1,4,7,10-tetraacetic acid (DOTA). These chelators are conjugated to the copolymer used in the formation of the micelles, as done for ^{111}In-DTPA-PEG-b-PCL micelles, demonstrating a higher tumor uptake and an increasing circulation half-life with the increase of PEG molecular weight [14]. The use of chelating agents contributes to higher stability, however, since they cause a chemical modification in the corona of the micelles, it is expectable that their biodistribution and pharmacokinetics are also affected [66].

In order to overcome this, recent studies have presented a new strategy for the radiolabeling of micelles, with the aim of allowing *in vivo* imaging without modifying the chemical structure of the nanoparticle. In this technique, the radionuclide is entrapped in the micellar core, by forming a complex with a hydrophobic substance, such as 8-hydroxyquinoline or tropolone, exploiting the micelles ability to encapsulate hydrophobic compounds. The similarity between the hydrophobic radionuclide complexes and the hydrophobic drugs allows to indirectly extrapolate the biodistribution of a drug, since it is expected to behave similarly to the complex [12, 13].

Chapter 3

Materials and Methods

3.1 Solvents and reagents

All chemicals and solvents were of reagent grade and were used without additional purification unless otherwise stated.

Dimethyl sulfoxide (DMSO) was used after drying with 4 Å molecular sieves.

The water (H_2O) used for the experiments was ultrapure water by Water Purification Systems - MilliQ.

The copolymers Me-PEG-*b*-PCL and NH_2-PEG-*b*-PCL were already synthesized in the Radioparmaceutical Sciences Group (C^2TN/IST), as previously described [68]. The molecular weight of Me-PEG-*b*-PCL and NH_2-PEG-*b*-PCL is 10000 Da and 8000 Da, respectively.

The gold complex TBA[Au(cdc)$_2$] was already synthesized and characterized in the Solid State Group (C^2TN/IST) [5] and was kindly provided by Dulce Belo of C^2TN/IST. The molecular weight of TBA[Au(cdc)$_2$] is 671.76 g/mol.

A2780 (cisplatin sensitive), A2780cisR (cisplatin resistant) and OVCAR3 (cisplatin sensitive) ovarian cancer cells were purchased from Sigma-Aldrich. Cell media and media supplements were purchased from Gibco (Thermo Fisher Scientific).

^{111}InCl$_3$ (370 MBq/mL in HCl) was obtained from Mallinckrodt Medical B.V. (Netherlands).

3.2 Methods

UV-Vis spectrophotometry was performed on a Cary 60 UV-Vis spectrophotometer from *Agilent Technologie*s with quartz cuvettes (QS high Precision Cell; 10 mm (*Hellma*® *Analytics*)).

For the characterization of micelles, a Zetasizer Nano ZS from Malvern was used with zeta-potential cells.

^{1}H Nuclear Magnetic Resonance Spectroscopy (NMR) spectra were recorded in a Bruker Avance III 300 MHz instrument. Chemical shifts of ^{1}H (δ, ppm) are reported relative to the residual solvent peaks relative to tetramethylsilane (SiMe$_4$).

High Performance Liquid Chromatography (HPLC) analysis was performed on a Perkin Elmer Series 200 Pump coupled to a Perkin Elmer Series 200 UV-Vis Detector using as eluents H$_2$O with 0.1% of trifluoroacetic acid (TFA) (A) and acetonitrile with 0.1% TFA (B). The eluents were of HPLC grade and the aqueous solutions were prepared with ultrapure MilliQ water.

- **Analytical method**

Column: SUPELCO Analytical; Discovery® BIO Wide Pore 300 Å, C18; 25 cm x 4.6 mm, 5 μm (Sigma-Aldrich®)

Detection: λ = 303 nm

Flow: 1.0 mL/min

Eluents: A - H$_2$O - 0.1% TFA; B - ACN - 0.1% TFA

Table 3.1: HPLC method used for TBA[Au(cdc)$_2$]. The duration of the method was 15 minutes.

Step	Time	A% (H$_2$O - 0.1% TFA)	B% (ACN - 0.1% TFA)	Gradient
0	5	60	40	No
1	15	10	90	Yes

3.2.1 Synthesis of folate-PEG-*b*-PCL

Folic acid (FA) was first activated with N-hydroxysuccinimide (NHS) and dicyclohexylcarbodiimide (DCC) and then conjugated to the amino-terminated poly(ethylene glycol)-b-poly(ϵ-caprolactone) (NH$_2$-PEG-b-PCL).

200 mg (0.453 mmol) of FA were dissolved in 10 mL of dried DMSO and continuously stirred in nitrogen atmosphere at room temperature (RT) for 1 h. Then, 57.35 mg (0.498 mmol) of NHS and 102.80 mg (0.498 mmol) of DCC were added to the solution, corresponding to a FA:NHS:DCC molar ratio of 1:1.1:1.1. The mixture was maintained under stirring overnight in nitrogen atmosphere at RT. The by-product dicyclohexylurea was removed by centrifugation of the mixture at 2500 g for 10 minutes and washed with DMSO. To ensure that all the by-product was eliminated, the supernatant was collected and centrifuged once more at 2500 g for 10 minutes.

After the synthesis of the folate-NHS ester, 230 mg (28.75 μmol) of NH$_2$-PEG-b-PCL and 50 μL of triethylamine (Et$_3$N) were added to the activated folate and the reaction mixture was continuously stirred overnight in nitrogen atmosphere at RT and then lyophilized. To separate the free FA from the folate conjugated copolymer, 10 mL of acetonitrile were added and the mixture was centrifuged at 2500 g for 5 minutes to precipitate the free FA and washed with acetonitrile. Then, the supernatant was dried under nitrogen and lyophilized. The conjugated copolymer was analyzed by ^{1}H NMR and UV-Vis spectrophotometry.

3.2.2 Synthesis of the micelles

BCMs were synthesized by the thin-film hydration method [67]. For the preparation of BCMs and BCMs-Au(cdc)$_2$, 50 mg (5.00 μmol) of methoxy-terminated poly(ethylene glycol)-b-poly(ϵ-caprolactone) (Me-PEG-b-PCL) and 2 mg (2.98 μmol) of TBA[Au(cdc)$_2$] (for the loaded micelles) were dissolved in 4 mL of chloroform and, after 4 h under continuous stirring at RT, the solvent was evaporated under nitrogen, in order to form a thin film. After overnight evaporation with N$_2$, the film was then hydrated with 3 mL of MilliQ water at 60°C and sonicated for 1 h at 60°C. The mixture was then maintained under stirring for 3 h at RT. Afterwards, the solution was centrifuged at 1000 g for 10 min and the supernatant was lyophilized. Functionalized micelles were obtained using a method similar to the one previously described, with the incorporation of folate-PEG-b-PCL. Briefly, 25 mg (2.50 μmol) of Me-PEG-b-PCL, 6.5 mg of folate-PEG-b-PCL and 1.3 mg (1.94 μmol) of TBA[Au(cdc)$_2$] (for the loaded micelles) were used for the synthesis of BCMs-folate and BCMs-Au(cdc)$_2$-folate. The preparation of the micelles followed the same procedure described for the non functionalized micelles. A schematic representation of the experimental procedure for the synthesis of the BCMs is presented in Figure 3.1.
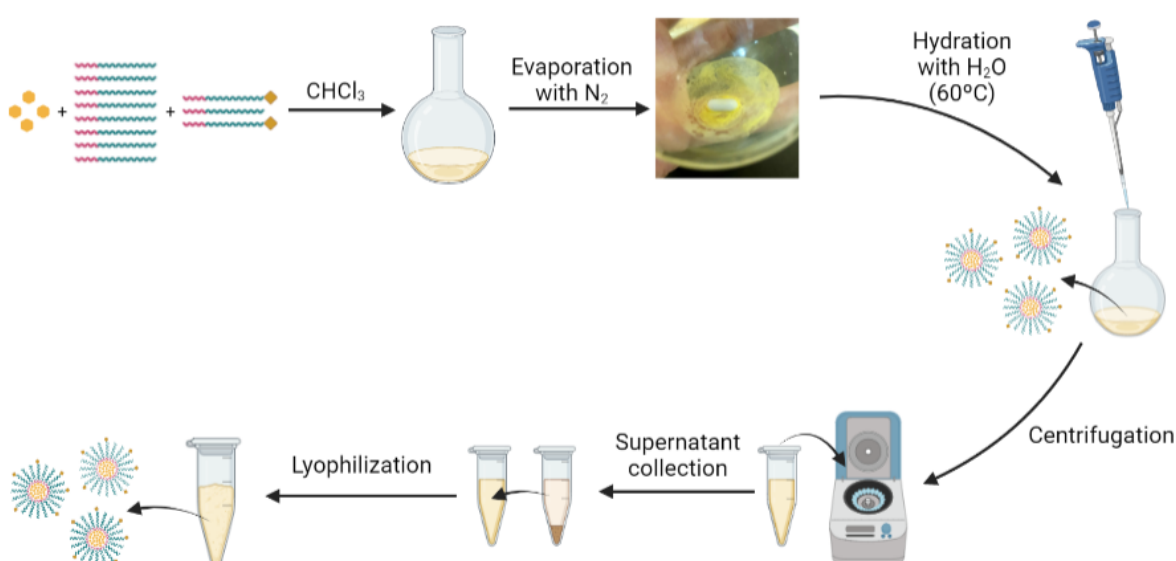
Figure 3.1: Experimental procedure for the synthesis of the micelles.

3.2.3 Characterization of the micelles

The hydrodynamic diameter (D_h) and zeta potential of micelles were determined using a Zetasizer Nano ZS from Malvern with zeta-potential cells. Before the measurement, the micelles were dissolved in MilliQ water in order to obtain 1 g/L solutions that were then sonicated. Afterwards, the micelles were diluted in order to obtain 0.1 g/L solutions and filtered using a 0.20 μm syringe filter. The particle size was measured by dynamic light scattering (DLS) at 25 °C with a 173° scattering angle and an optic arrangement known as non-invasive back scatter (NIBS). All measurements were repeated three times.

The [Au(cdc)$_2$]$^-$ loading content (LC) and loading efficiency (LE) were estimated by UV-Vis spectrophotometry by measuring the absorbance at 303 nm with reference to a calibration curve established for the gold compound. For this, 2-3 mg of BCMs-Au(cdc)$_2$ or BCMs-Au(cdc)$_2$-folate were dissolved in 1 mL of acetonitrile, vortexed and centrifuged at 3000 g for 10 minutes to precipitate the copolymer. Then, the supernatant was collected and analyzed by UV-Vis spectrophotometry.

The LC was calculated by the ratio of [Au(cdc)$_2$]$^-$ entrapped within the micelles over the total amount of micelles and LE was calculated by the ratio of entrapped [Au(cdc)$_2$]$^-$ over the total amount of TBA[Au(cdc)$_2$] used to prepare the micelles [67].

The presence of FA in the functionalized micelles was confirmed by UV-Vis spectrophotometry. For this, the micelles were dissolved in acetonitrile and analyzed. For the loaded micelles (BCMs-Au(cdc)$_2$-folate), the [Au(cdc)$_2$]$^-$ was removed using 3 kDa Amicon centrifugal filters, following the procedure shown in Figure 3.2, before the analysis. The solution of micelles in 500 μL of acetonitrile was placed in the Amicon filter and centrifuged at 14000 g for 30 minutes. Afterwards, 500 μL of acetonitrile were added to the filter and centrifuged in the same conditions. Then, the Amicon filter was placed upside down and the retentate was recovered by centrifuging at 2000 g for 2 minutes.
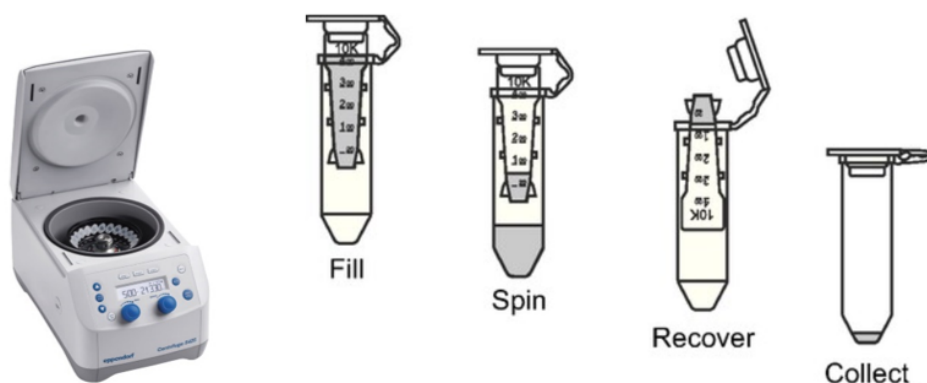
Figure 3.2: Experimental procedure for the use of an Amicon centrifugal filter. Adapted from [69, 70].

The stability of the gold complex encapsulated in the micelles was evaluated by HPLC and UV-Vis spectrophotometry. For this, BCMs-Au(cdc)$_2$ or BCMs-Au(cdc)$_2$-folate were dissolved in acetonitrile,

vortexed and centrifuged at 3000 g for 10 minutes to precipitate the copolymer. Then, the supernatant was collected and analyzed. The free TBA[Au(cdc)$_2$] was also analyzed.

3.2.4 *In vitro* [Au(cdc)$_2$]$^-$ release study

The *in vitro* release of [Au(cdc)$_2$]$^-$ from BCMs-Au(cdc)$_2$ and BCMs-Au(cdc)$_2$-folate was evaluated at pH 7.4 and pH 5.5 using the dialysis method [71, 72]. Briefly, a solution of 3 mg of BCMs-Au(cdc)$_2$ or BCMs-Au(cdc)$_2$-folate in 3 mL of 0.01 M phosphate buffer saline (PBS) pH 7.4 was placed in a regenerated cellulose tubular dialysis membrane (MWCO = 25 kDa), immersed into 200 mL of 0.01 M PBS pH 7.4 or pH 5.5 and maintained at 37°C under continuous stirring. At predetermined time points, 500 µL of the solution inside the dialysis membrane were retrieved and lyophilized and the membrane was immersed in fresh medium. Afterwards, 500 µL of acetonitrile were added to the lyophilized solutions and the resultant solutions were vortexed and centrifuged at 3000 g for 10 minutes to precipitate the copolymer and the PBS salts. The supernatant was collected and analyzed by UV-Vis spectrophotometry. The drug release profile was calculated as the percentage of released [Au(cdc)$_2$]$^-$ *versus* time, in which the 100% release corresponds to the total amount of [Au(cdc)$_2$]$^-$ entrapped in the micelles.

3.2.5 Antiproliferative activity

The cytotoxic activity of TBA[Au(cdc)$_2$], BCMs, BCMs-Au(cdc)$_2$, BCMs-folate and BCMs-Au(cdc)$_2$-folate was evaluated in ovarian cancer cell lines, namely the cisplatin-sensitive A2780 and OVCAR3 cell lines and the cisplatin-resistant A2780cisR cell line. Cells were grown in RPMI medium supplemented with 10% fetal bovine serum (FBS) and 1% of a mixture of penicillin and streptomycin and maintained in a humidified incubator (Heraeus, Germany) with 5% CO$_2$. A MTT assay was performed to evaluate the cellular viability (Figure 3.3). For the assay, cells were seeded in 96-well plates and were allowed to adhere for 24 h. The loaded micelles (BCMs-Au(cdc)$_2$), with a loading content of 3.7% were diluted to prepare serial concentrations corresponding to 0.01-40 µM of [Au(cdc)$_2$]$^-$ and the loaded micelles functionalized with folic acid (BCMs-Au(cdc)$_2$-folate), with a loading content of 3.0% were diluted to prepare serial concentrations corresponding to 0.01-30 µM of [Au(cdc)$_2$]$^-$. Non-loaded micelles (BCMs and BCMs-folate) were diluted to prepare serial concentrations equivalent to that used in the loaded micelles. All the micelles were diluted in RPMI medium without folate, supplemented with 5% FBS and 1% of a mixture of penicillin and streptomycin. The micelles and the free gold complex were added to the cells and incubated for 48 h at 37°C. Afterwards, the medium was discarded and 200 µL of MTT solution in PBS (0.5 mg/mL) were added to each well and maintained for 3 h at 37°C. Then, the medium was removed and 200 µL of DMSO were added to the cells to solubilize the formazan crystals. The cellular viability (expressed in %) was assessed in a plate

spectrophotometer (Power Wave Xs, Bio-Tek), by measuring the absorbance at 570 nm. The IC_{50} values were calculated using the GraphPad Prism software (version 5.0). Results are shown as the mean $\pm$ SD of one experiment done with at least three replicates each.
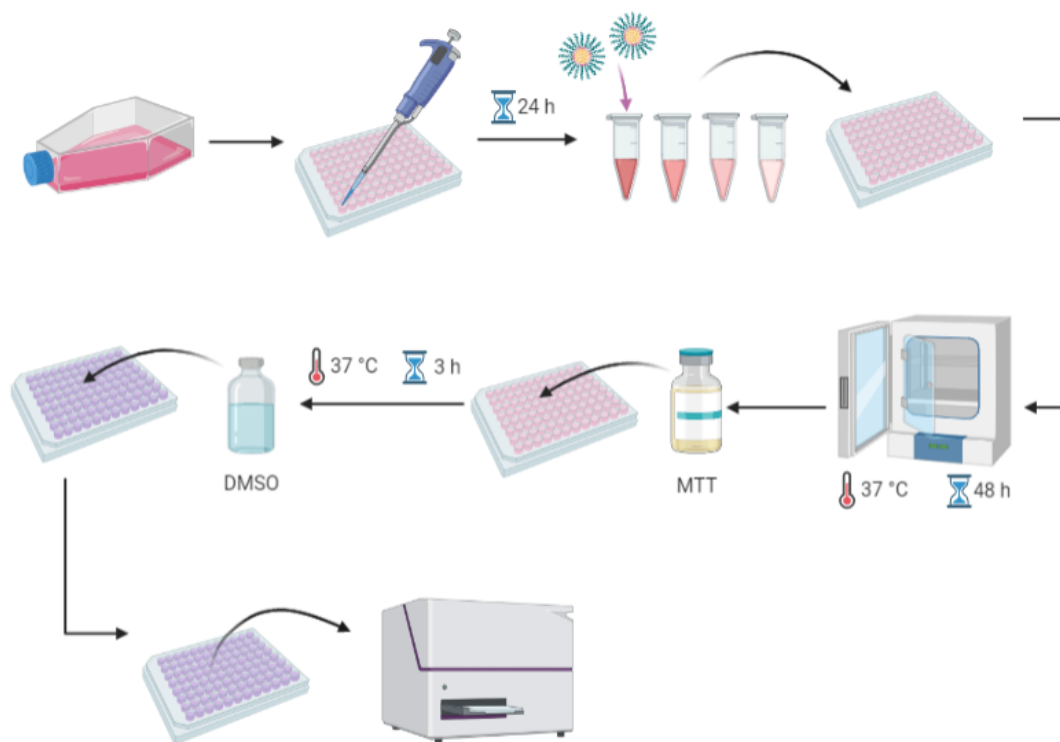
Figure 3.3: Experimental procedure for the determination of the cytotoxic activity of the micelles.

3.2.6 Radiolabeling with [111]In

The manipulation of all radioactive compounds was performed in a dedicated laboratory following the radiation protection rules. Activities were measured in a gamma counter (Berthold, LB2111, Germany).

The loaded micelles (BCMs-Au(cdc)$_2$ and BCMs-Au(cdc)$_2$-folate) were labeled with ^{111}In-oxine.

3.2.6.1 Preparation of ^{111}In-oxine

The synthesis of ^{111}In-oxine was performed as previously reported [73].

Briefly, 50 μL of a 2 g/L solution of 8-hydroxyquinoline in ethanol were mixed with 200 μL of 0.4 M acetate buffer pH 5 and [111]InCl$_3$ (6.29 MBq) in 0.01 M HCl, vortexed and left for 5 minutes at RT. Then, 500 μL of dichloromethane (DCM) were added, vortexed and the DCM was removed. Afterwards,

300 μL of 0.4 M acetate buffer pH 5 were added and the solution was centrifuged at 1500 g for 3 minutes. The aqueous phase was removed and the solution was dried under nitrogen.

The purity of the complex was evaluated by Instant Thin Layer Chromatography in Silica Gel (ITLC-SG) using a mixture of CHCl$_3$/MeOH (90:10) as eluents (Rf ([111]InCl$_3$) = 0.0, Rf (^{111}In-oxine) = 0.9 - 1).

3.2.6.2 Micelles labeling with ^{111}In-oxine

1 mg of BCMs-Au(cdc)$_2$ or BCMs-Au(cdc)$_2$-folate was dissolved in 1 mL of 0.01 M PBS pH 7.4, vortexed and sonicated for 20 minutes. Then, 450 μL of the solution were added to the ^{111}In-oxine, vortexed and sonicated for 20 minutes at 40°C.

The radiolabeled micelles (^{111}In-BCMs-Au(cdc)$_2$ and ^{111}In-BCMs-Au(cdc)$_2$-folate) were purified using 10 kDa Amicon centrifugal filters, following the procedure shown in Figure 3.2. The solution was placed in the Amicon filter and centrifuged at 14000 g for 10 minutes. Afterwards, 300 μL of PBS were added and the solution was centrifuged again in the same conditions. Then, the Amicon filter was placed upside down and the retentate was recovered by centrifuging at 2000 g for 2 minutes. The activity in the filter and in the filtrate were measured.

3.2.7 *In vitro* stability studies

The stability of ^{111}In-labeled micelles was evaluated at 37°C in 0.01 M PBS pH 7.4 and in cell culture medium (RPMI). For this study, 300 μL of PBS and RPMI were introduced, respectively, in 10 kDa Amicon centrifugal filters. Then, 30 μL of ^{111}In-BCMs-Au(cdc)$_2$ or ^{111}In-BCMs-Au(cdc)$_2$-folate were added to each filter and left at 37°C. At different time points (24 h, 48 h, 72 h), the filters were centrifuged at 14000 g for 10 minutes and the filtrate was collected. The activity in the retentate and in the filtrate was measured. Afterwards, 300 μL of PBS and RPMI were introduced, respectively, in each filter and left at 37°C until the next time point.

Chapter 4

Results and discussion

As described in Chapter 2.2, a recent study evaluated the cytotoxic and antimicrobial activity of monoanionic gold (III) bisdithiolate complexes, with promising results [5]. The $[Au(cdc)_2]^-$, whose molecular structure is presented in Figure 2.1, in particular, displayed significant cytotoxic activity against cisplatin-sensitive A2780 and cisplatin-resistant A2780cisR ovarian cancer cell lines. Thus, this complex was further explored in this thesis, by evaluating its behavior when its solubility is increased by encapsulating it in BCMs.

The TBA[Au(cdc)$_2$] (MW = 671.76 g/mol) was already synthesized by the Solid State Group (C^{2}TN/IST). The complex was characterized by UV-Vis spectrophotometry and HPLC after being solubilized with acetonitrile.

The UV-Vis spectrum shows an absorption band at 303 nm (Figure 4.1). This wavelength was selected for the UV detection of the HPLC method.
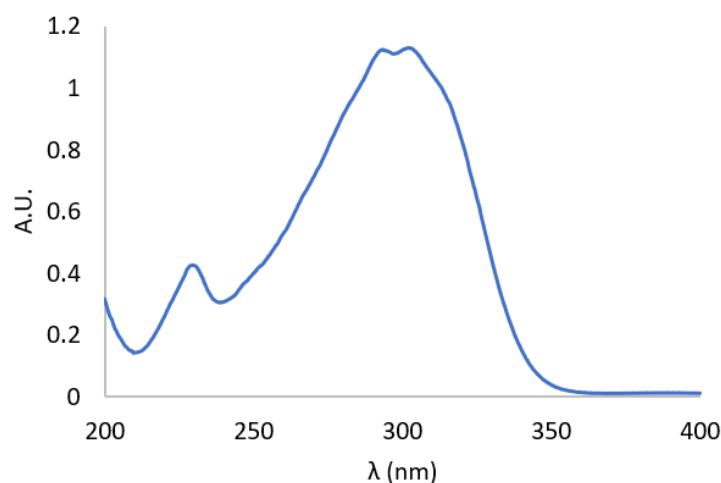
Figure 4.1: UV-Vis spectrum of TBA[Au(cdc)$_2$].

The HPLC analysis was performed with H$_2$O - 0.1% TFA and ACN - 0.1% TFA as eluents. The

HPLC chromatogram (Figure 4.2) shows a single peak at a retention time of 12.3 min, indicating that there are no other species that absorb at 303 nm. This retention time indicates that the complex elutes at a solvent composition of 20% of H_2O - 0.1% TFA and 80% of ACN - 0.1% TFA.
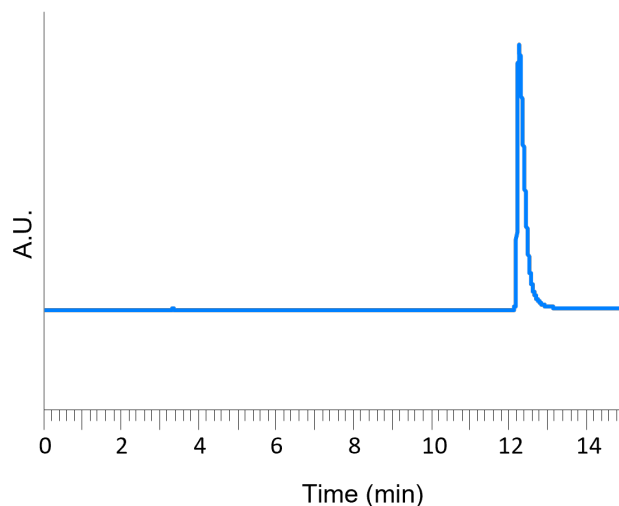
Figure 4.2: HPLC chromatogram of TBA[Au(cdc)$_2$] (R_t = 12.3 min) with UV Detection at λ = 303 nm.

BCMs are composed by amphiphilic copolymers that self assemble in aqueous medium, as further explained in Chapter 2.3.1. For this work, the block copolymer used was the Me-PEG-b-PCL, one of the most widely used [67, 74], which has PEG as the hydrophilic block, forming the shell of the micelle, and polycaprolactone (PCL) as the hydrophobic block, forming the core, as seen in Figure 4.3.
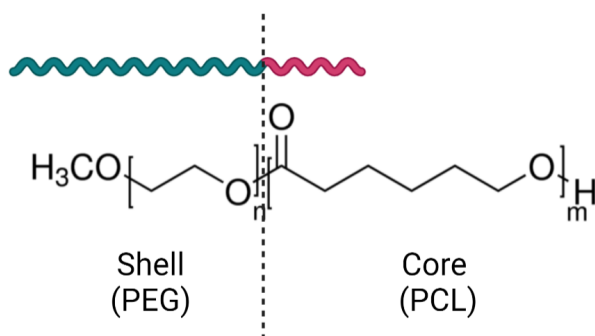
Figure 4.3: Molecular structure of Me-PEG-b-PCL

The Me-PEG-b-PCL was already synthesized by the Radiopharmaceutical Sciences Group (C^{2}TN/IST) by metal-free cationic ring-opening polymerization of ϵ-caprolactone. The molecular weight and chemical composition of the copolymer were assessed based on the number of caprolactone monomers (ca. 45), determined by ^{1}H-NMR and the molecular weight of the PEG precursor (5000 Da). The estimated molecular weight of Me-PEG-b-PCL is 10000 Da [68].

4.1   Synthesis and characterization of the micelles

The non-loaded micelles (BCMs), as well as the respective $[Au(cdc)_2]^-$ loaded congener (BMCs-Au(cdc)$_2$) were prepared by the thin-film hydration method [67]. As can be seen in Figure 4.4, the $[Au(cdc)_2]^-$ is entrapped in the hydrophobic core during the self-assembly of the micelles, due to its poor water solubility.
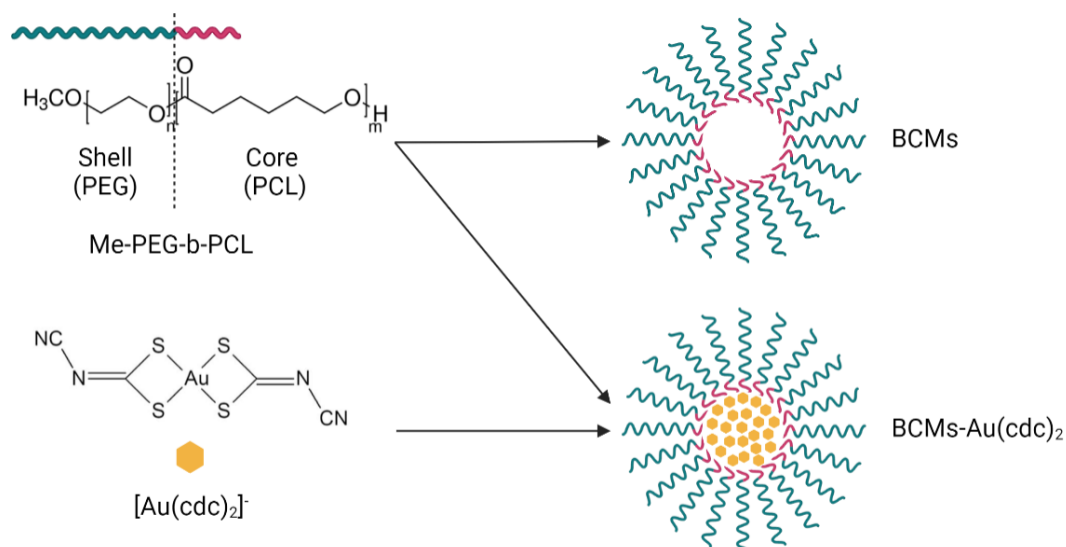
Figure 4.4: Synthesis of the non-functionalized micelles. BCMs correspond to the non-loaded micelles and BCMs-Au(cdc)$_2$ correspond to the loaded micelles.

For the synthesis of the micelles, the copolymer Me-PEG-b-PCL and the gold complex TBA[Au(cdc)$_2$] (for the loaded micelles) are dissolved in chloroform, followed by the evaporation of the solvent to create a thin-film. Afterwards, the film is hydrated with H_2O, causing the self-assembly of the copolymer, creating the micelles. Then, the micelles are centrifuged at 1000 g for 10 minutes and the supernatant is collected and lyophilized.

The D_h and the zeta potential of the micelles were determined by DLS (Dynamic Light Scattering) and LDV (Laser Doppler Velocimetry), respectively, after diluting the samples with ultrapure water to obtain 0.1 g/L solutions and filtering them with a 0.20 μm syringe filter.

For micelles, the D_h must be below 200 nm for the nanoparticles to have a prolonged circulation half-life in the blood [37]. The polydispersity index (PDI) is an indicator of the homogeneity of the samples in terms of particles and can vary between 0 and 1, with values closer to 0 indicating higher homogeneity [75]. The zeta potential presents a measure of the repulsion between the charged particles, with values lower than -30 mV or higher than 30 mV considered ideal, indicating that the particles present enough charge to prevent aggregation, due to electrostatic repulsion. Particles with values outside of this are more prone to particle aggregation and flocculation [76, 77].

The $[Au(cdc)_2]^-$ LC and LE were determined with reference to a standard calibration curve established for the gold complex (Figure 4.5) (*vd Appendix A.1* to consult the values).
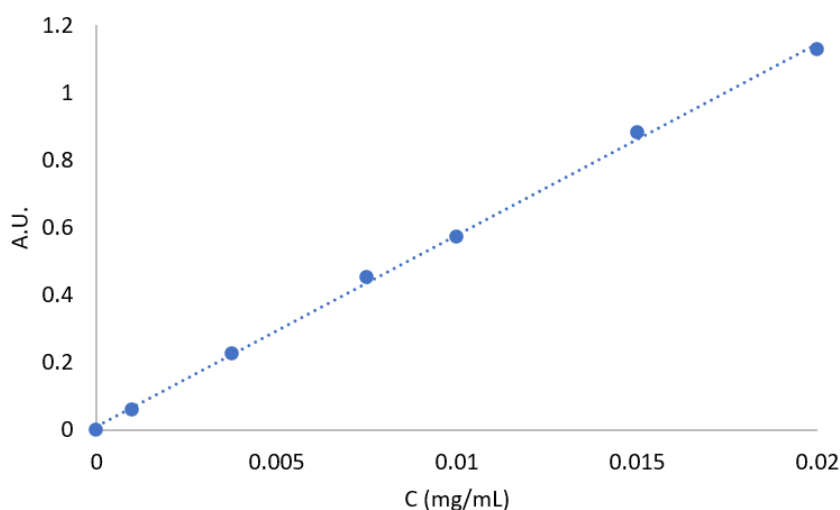
Figure 4.5: Calibration curve of TBA[Au(cdc)$_2$] at λ = 303 nm.

The calibration curve was plotted and the regression line equation and correlation coefficient (R^2) were calculated (Equation 4.1) (*vd Appendix A.2*).

$$Abs = 56.848 \times C + 0.00854 \tag{4.1}$$

$$R^2 = 0.999$$

The drug LC and LE were calculated using the calibration curve to obtain the corresponding amount of gold complex encapsulated for a specific amount of micelles, and then recurring to Equation 4.1. Briefly, 2-3 mg of BCMs-Au(cdc)$_2$ were dissolved in 1 mL of acetonitrile, vortexed and centrifuged at 3000 g for 10 minutes to precipitate the copolymer. Then, the supernatant was collected and analyzed by UV-Vis spectrophotometry to obtain the absorption intensity at λ = 303 nm.

The $[Au(cdc)_2]^-$ LC and LE were calculated using Equations 4.2 and 4.3, respectively.

$$LC\ (mg_{[Au(cdc)_2]^-}/g_{BCM}) = \frac{\text{weight of } [Au(cdc)_2]^- \text{entrapped within the micelles}}{\text{total weight of micelles}} \tag{4.2}$$

$$LE\ (\%) = \frac{\text{weight of } [Au(cdc)_2]^- \text{ entrapped within the micelles}}{\text{total weight of } [Au(cdc)_2]^- \text{ used}} \times 100 \tag{4.3}$$

4.1.1 Optimization of the hydration step

The hydration step is essential for a successful micellization of the copolymer. As a preliminary study, the conditions of this step were optimized. On a first approach, the thin film was hydrated with MilliQ water at 60°C with agitation and the solution was left for 4 h at RT, however, the LC obtained was of approximately 6 mg$_{[Au(cdc)_2]^-}$/g$_{BCM}$. Then, different parameters were changed, such as the stirring velocity, the type of water used (ultrapure or distilled), the solvent used in the hydration (H$_2$O or PBS) and the centrifugation speed, however, the LC obtained in these studies was between 5 and 11 mg$_{[Au(cdc)_2]^-}$/g$_{BCM}$, demonstrating that these parameters do not affect the formation of the micelles significantly.

Afterwards, maintaining the experimental procedure of the first study, the solution of the micelles was sonicated at 60°C after the ultrapure water was added and then left for 3 h at RT with continuous stirring. This study was performed with 20 minutes and 1 h of sonication, in order to analyze the effect of ultrasound in the D$_h$, PDI, zeta potential, LC and LE of the micelles. The results of this optimization process are presented in Table 4.1

Table 4.1: Hydrodynamic diameter (D$_h$), Polydispersity index (PDI), Zeta potential, Loading Content (LC) and Loading Efficiency (LE) of the micelles for different sonication times.

Sonication time (min)	D$_h{}^a$ (nm)	PDI	Zeta potential (mV)	LC (mg$_{[Au(cdc)_2]^-}$/g$_{BCM}$)	LE (%)
0	58.3 ± 7.7	0.32 ± 0.06	-58.0 ± 2.25	6.1	5.4
20	80.3 ± 3.3	0.21 ± 0.02	-51.8 ± 1.50	12.1	24.2
60	99.4 ± 4.3	0.33 ± 0.01	-53.6 ± 0.30	37.0	88.9

^{a} Mean±SD of distribution by number (refractive index = 1.5)

With this optimization process, it was possible to observe that the sonication at 60°C is essential to facilitate the micellization and the encapsulation of the gold complex, with the LC increasing as the sonication time increases. It can also be verified that the D$_h$ increases with sonication, which presents a disadvantage however, for 1 h of sonication, the D$_h$ is below 100 nm, which remains suitable for these nanoparticles. Based on these results, all the micelles used for the remaining studies were sonicated for 1 h at 60°C after the hydration of the film with ultrapure MilliQ H$_2$O and then left for 3 h at RT with continuous stirring.

4.1.2 Characterization of non-loaded and [Au(cdc)$_2$]$^-$-loaded micelles

The results obtained for the D$_h$, PDI, zeta potential, LC and LE of the non-loaded and [Au(cdc)$_2$]$^-$-loaded micelles are summarized in Table 4.2.

Table 4.2: Hydrodynamic diameter (D_h), Polydispersity index (PDI), Zeta potential, Loading Content (LC) and Loading Efficiency (LE) of the micelles.

Micelles	$D_h{}^a$ (nm)	PDI	Zeta potential (mV)	LC $(mg_{[Au(cdc)_2]^-}/g_{BCM})$	LE (%)
BCMs	150.9 ± 6.6	0.29 ± 0.01	-44.0 ± 0.26	-	-
BCMs-Au(cdc)$_2$	99.4 ± 4.3	0.33 ± 0.01	-53.6 ± 0.30	37.0	88.9

^{a} Mean$\pm$SD of distribution by number (refractive index = 1.5)

The micelles present a D_h below 200 nm, contributing to a long circulation half-life, a PDI suggesting that the samples were homogeneous in terms of size, with values similar to the ones found in the literature [2, 3] and zeta potential values indicating high stability of the micelles, with low tendency to form aggregates. These micelles were obtained with high LC and LE, suggesting that there is a good compatibility between the gold complex and the core of the micelles.

The DLS histograms (Figure 4.6) show a monomodal size distribution.
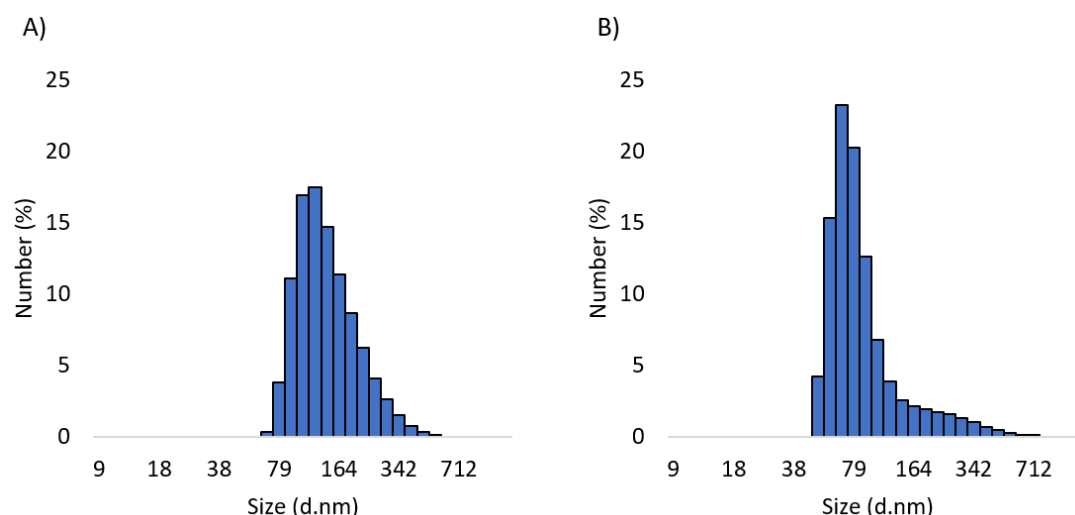
Figure 4.6: DLS histograms of A) BCMs and B) BCMs-Au(cdc)$_2$.

The stability of the gold complex encapsulated in the micelles was evaluated by UV-Vis and HPLC. For this, the loaded micelles (BCMs-Au(cdc)$_2$) were disassembled with acetonitrile, centrifuged to precipitate the copolymer and the supernatant was collected and analyzed.

Figure 4.7 shows that the free gold complex (TBA[Au(cdc)$_2$]) and the complex collected from the loaded micelles (BCMs-Au(cdc)$_2$) presented similar absorption spectra, with an absorption band at 303 nm, characteristic of [Au(cdc)$_2$]$^-$.
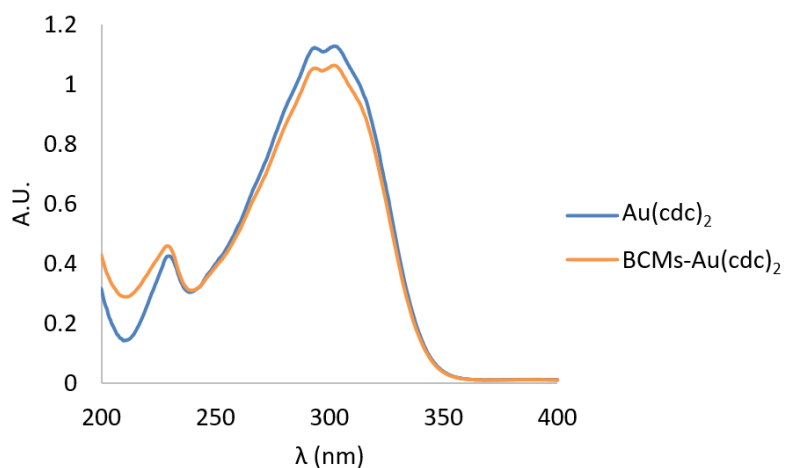
Figure 4.7: UV-Vis spectra of TBA[Au(cdc)$_2$] and BCMs-Au(cdc)$_2$.

The HPLC chromatograms (Figure 4.8) show that the free gold complex and the gold complex collected from the loaded micelles exhibit similar chromatographic profiles, with similar retention times, suggesting that the complex maintains its chemical structure unaltered, without suffering degradation after being encapsulated in the micelles.
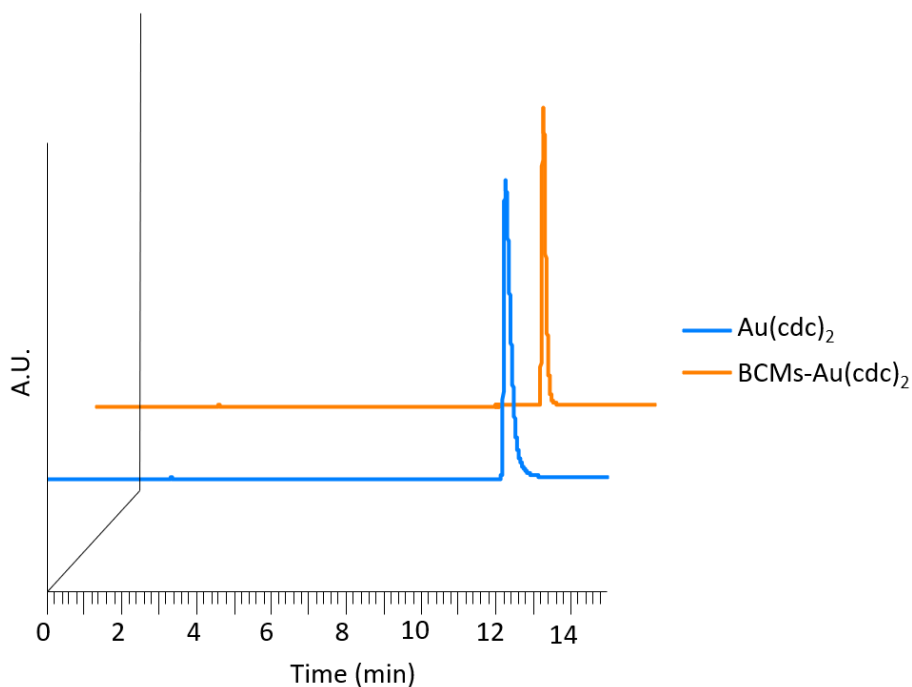
Figure 4.8: HPLC chromatograms of TBA[Au(cdc)$_2$] (R$_t$ = 12.3 min) and BCMs-Au(cdc)$_2$ with UV detection at λ = 303 nm.

4.2   Functionalization of the micelles with folic acid

With the aim of increasing selectivity and therefore, improve therapeutic efficacy with less toxicity, the surface of the micelles was decorated with folic acid. As further explained in Chapters 2.1 and 2.3.1, this ligand has high affinity to FRα, which is overexpressed in ovarian cancer. With the presence of folic acid in the outer shell, the micelles will bind to folate receptors present in ovarian cancer cells and will be internalized in the cell by receptor-mediated endocytosis, releasing their cargo inside the cell.

For the functionalization of the surface of the micelles, a folate-conjugated copolymer was synthesized to be added in the formulation of the micelles.

4.2.1   Synthesis and characterization of the folate-conjugated copolymer

The folate-conjugated copolymer was synthesized in two steps. First, the γ-carboxylic group of folic acid was activated with NHS and DCC (Figure 4.9). As can be seen in Figure 4.9, FA has two carboxylic groups (α and γ), however, the γ-carboxylic group has higher reactivity, being selectively activated [78].
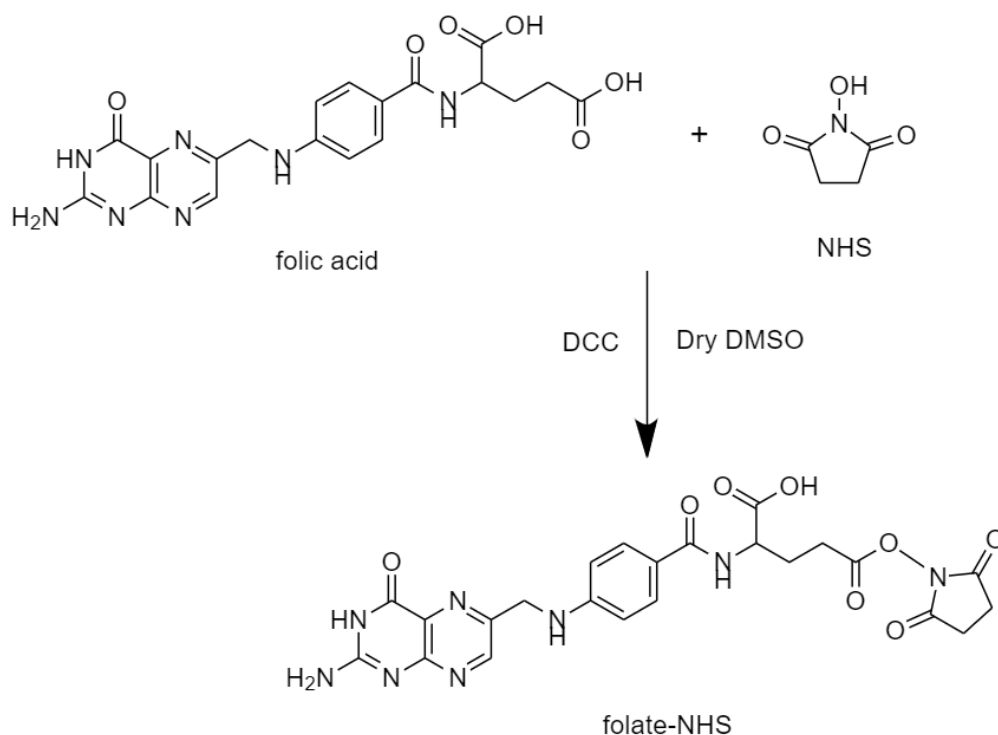
Figure 4.9: Synthesis of folate-NHS ester.

The activated ester was then reacted with NH$_2$-PEG-b-PCL, forming the copolymer folate-PEG-b-PCL (Figure 4.10). The NH$_2$-PEG-b-PCL copolymer was already synthesized by the

Radiopharmaceutical Sciences Group (C^{2}TN/IST) following a similar method to the one used for the synthesis of Me-PEG-*b*-PCL [68]. The estimated molecular weight of NH$_2$-PEG-*b*-PCL was 8000 Da.

Since an excess of FA was used, after lyophilization of the resultant solution, the free FA was removed by adding acetonitrile and centrifuging, since the acetonitrile can solubilize the copolymer, while the free FA remains insoluble.
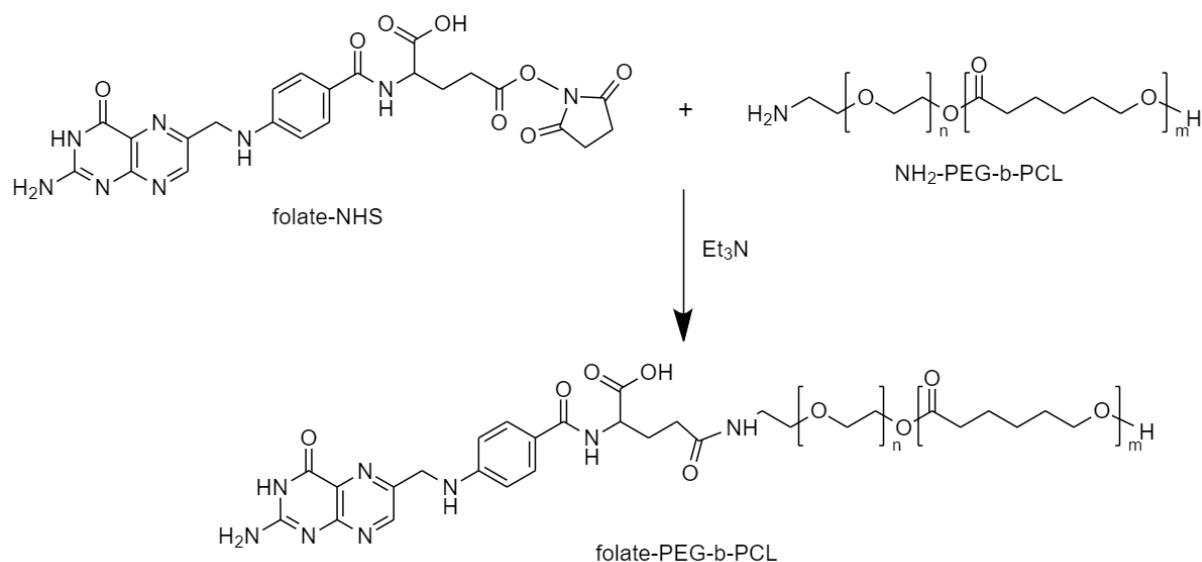
Figure 4.10: Synthesis of folate-PEG-*b*-PCL.

The presence of folic acid in the surface of the copolymer was confirmed by UV-Vis spectrophotometry (Figure 4.11) and ^{1}H NMR (Figure 4.12).

From the FA UV-Vis spectrum, it is possible to observe an absorption band at 288 nm. In the copolymer NH$_2$-PEG-*b*-PCL there is no significant absorption in the analyzed wavelength, while in the final copolymer functionalized with FA, the spectrum shows an absorption band at 288 nm, which is indicative that the conjugation was successful.
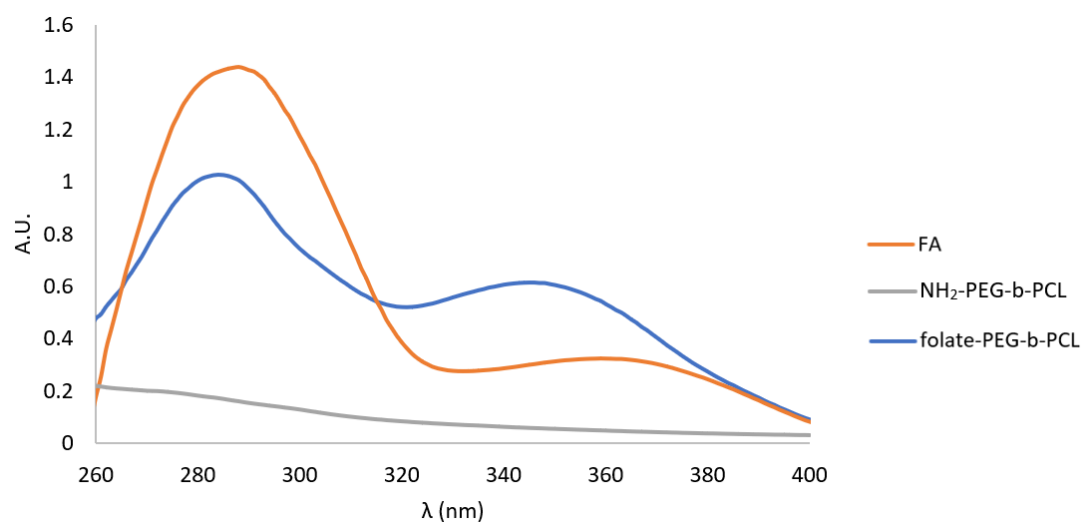
Figure 4.11: UV-Vis spectra of FA, NH$_2$-PEG-b-PCL and folate-PEG-b-PCL.

In the ^{1}H NMR spectrum of folate-PEG-b-PCL, the signals attributed to PEG-b-PCL are identified. In the aromatic region it is possible to identify the characteristic peaks of folate, similarly to what can be found in the literature [79, 80], verifying that the folate is conjugated to the copolymer.
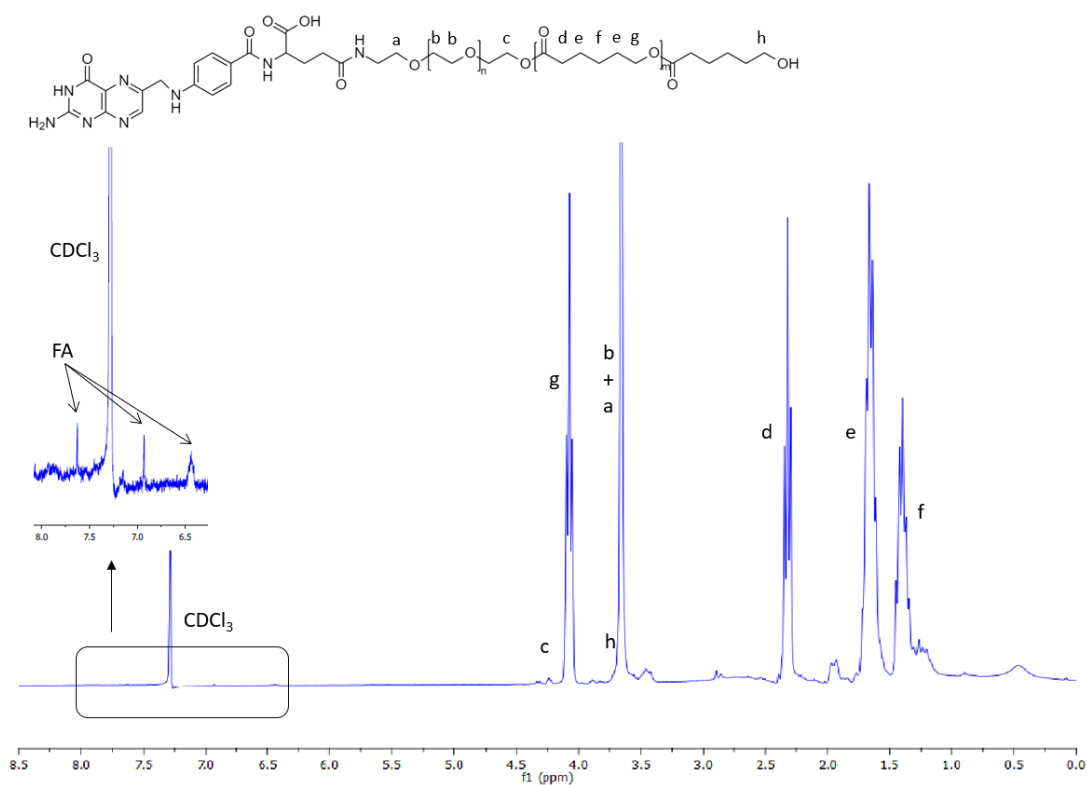
Figure 4.12: Structure and ^{1}H NMR spectrum of folate-PEG-b-PCL in CDCl$_3$, where n refers to the number of ethylene oxide repeat units and m to the number of caprolactone repeat units.

4.2.2 Synthesis and characterization of the functionalized micelles

The folate-containing micelles, non-loaded (BCMs-folate) and $[Au(cdc)_2]^-$-loaded (BCMs-Au(cdc)$_2$-folate) were prepared following the same method used for the non-functionalized micelles with the additional copolymer folate-PEG-b-PCL (Figure 4.13).
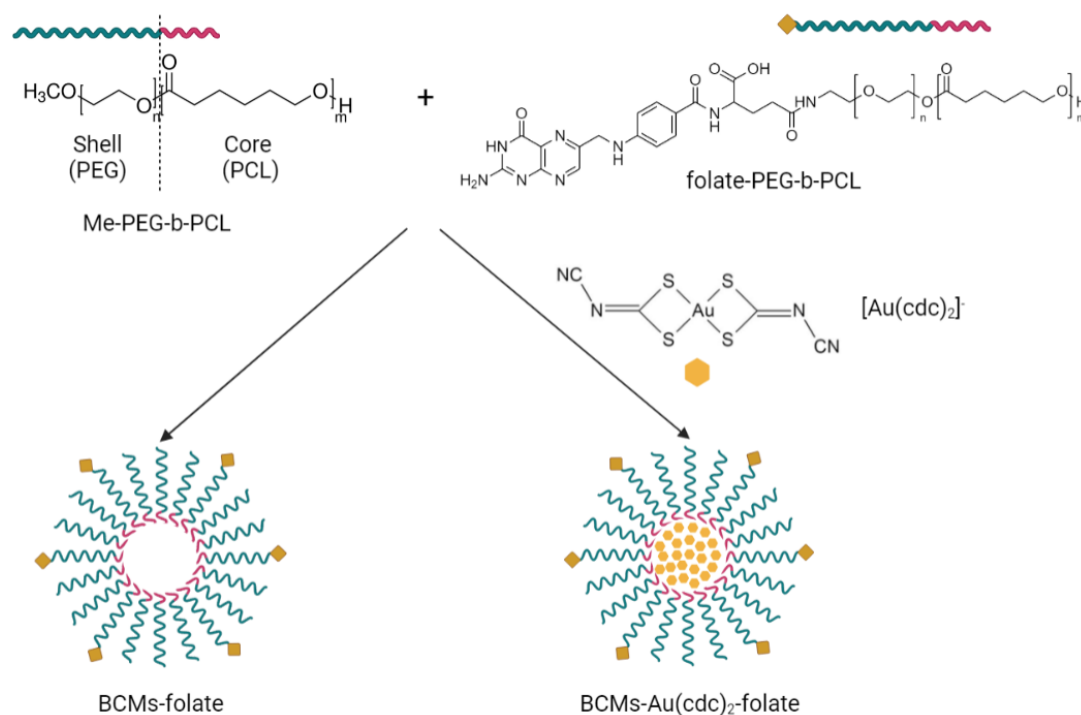
Figure 4.13: Synthesis of the functionalized micelles. BCMs-folate correspond to the functionalized non-loaded micelles and BCMs-Au(cdc)$_2$-folate correspond to the functionalized loaded micelles.

The results obtained for the D_h, PDI, zeta potential, LC and LE of the functionalized micelles are summarized in Table 4.3.

Table 4.3: Hydrodynamic diameter (D_h), Polydispersity index (PDI), Zeta potential, Loading Content (LC) and Loading Efficiency (LE) of the functionalized micelles.

Micelles	$D_h{}^a$	PDI	Zeta potential	LC	LE
	(nm)		(mV)	$(mg_{[Au(cdc)_2]^-}/g_{BCM})$	(%)
BCMs-folate	85.5 ± 2.7	0.25 ± 0.01	-53.1 ± 1.55	-	-
BCMs-Au(cdc)$_2$-folate	121.9 ± 4.2	0.19 ± 0.01	-55.6 ± 1.01	30.0	55.0

^{a} Mean±SD of distribution by number (refractive index = 1.5)

The functionalized micelles presented D_h similar to the ones obtained for the non-functionalized micelles. Comparing the results from Tables 4.2 and 4.3, it can be concluded that the values obtained for

non-loaded and loaded micelles do not allow to reach a conclusion regarding the effect of micelle loading on their size, since in the case of non-functionalized micelles the D_h decreases from 150.9 ± 6.6 nm (BCMs) to 99.4 ± 4.3 nm (BCMs-Au(cdc)$_2$), while in the functionalized micelles, this value increases from 85.5 ± 2.7 nm (BCMs-folate) to 121.9 ± 4.2 nm (BCMs-Au(cdc)$_2$-folate). For non-functionalized and functionalized micelles, it is also not possible to establish any trend, since for the loaded micelles the D_h decreases from 150.9 ± 6.6 nm (BCMs) to 85.5 ± 2.7 nm (BCMs-folate), while for the non-loaded micelles it increases from 99.4 ± 4.3 nm (BCMs-Au(cdc)$_2$) to 121.9 ± 4.2 nm (BCMs-Au(cdc)$_2$-folate).

The PDI and zeta potential values are also similar for both non-functionalized and functionalized micelles, demonstrating the homogeneity of the samples in terms of particle size and the high stability of the micelles.

The LC and LE of this micelles were slightly lower than that of non-functionalized micelles, most likely due to the presence of the folate-functionalized copolymer in the formulation of the micelles.

The DLS histograms (Figure 4.14) of the folate-containing micelles showed a monomodal size distribution, similarly to the ones that did not contain folic acid.
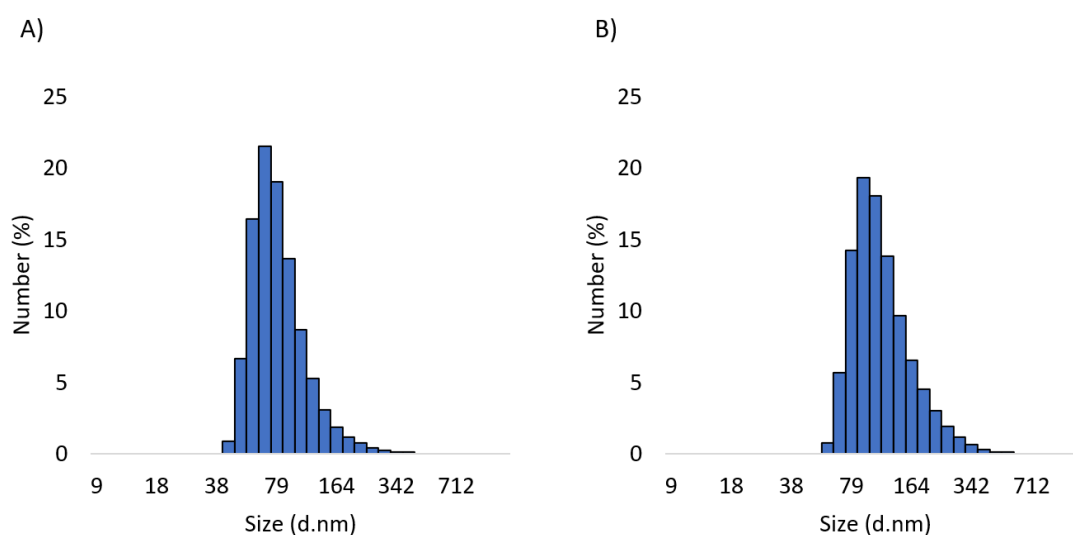
Figure 4.14: DLS histograms of A) BCMs-folate and B) BCMs-Au(cdc)$_2$-folate.

For the functionalized non-loaded and loaded micelles (BCMs-folate and BCMs-Au(cdc)$_2$-folate), it was necessary to confirm the presence of folic acid. As shown in Figure 4.11, FA has an absorption band at 288 nm. To ensure that the functionalization was successful, the micelles were disassembled with acetonitrile, and the resulting solution was analyzed by UV-Vis spectrophotometry. For the loaded micelles (BCMs-Au(cdc)$_2$-folate), the gold complex was removed using 3 kDa Amicon centrifugal filters and the micelles were analyzed afterwards. The UV-Vis absorption spectra of BCMs-folate and BCMs-Au(cdc)$_2$-folate are presented in Figure 4.15. Both spectra show an absorption band at 288 nm, characteristic of FA, verifying the presence of FA in the micelles.

A)

B)
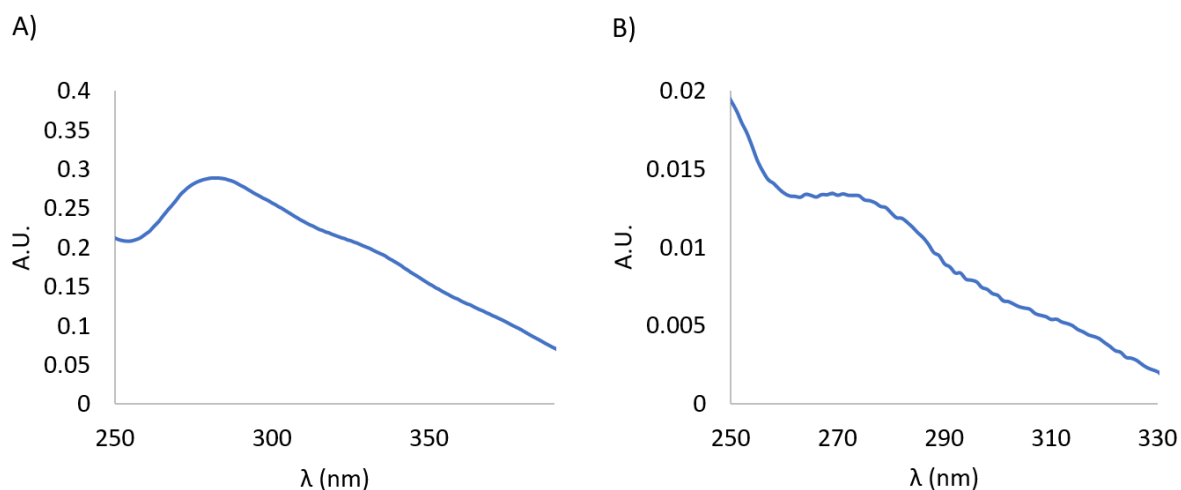
Figure 4.15: Confirmation of the presence of folic acid in A) BCMs-folate and B) BCMs-Au(cdc)$_2$-folate.

The stability of the gold complex encapsulated in the folate-containing micelles was evaluated by UV-Vis and HPLC. For this, the loaded micelles (BCMs-Au(cdc)$_2$-folate) were analyzed after the disassembly with acetonitrile.

The free gold complex and the complex collected from the micelles presented similar absorption spectra (Figure 4.16), with an absorption band at 303 nm, as observed for BCMs-Au(cdc)$_2$.
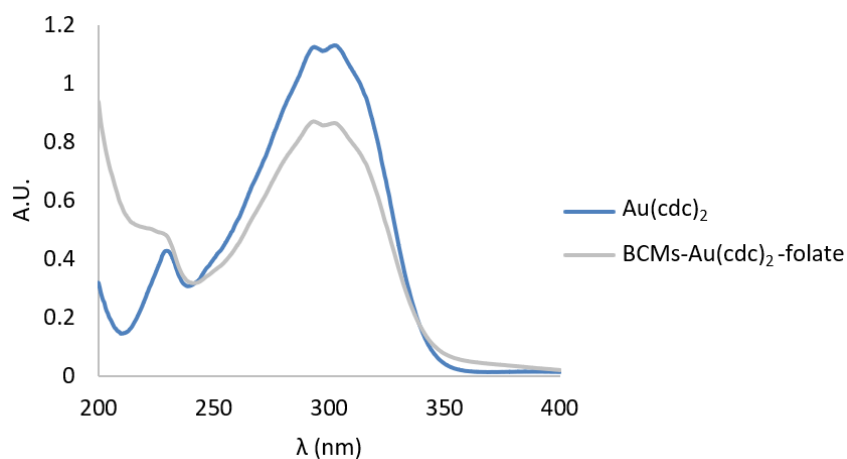
Figure 4.16: UV-Vis spectra of TBA[Au(cdc)$_2$] and BCMs-Au(cdc)$_2$-folate.

The HPLC chromatograms (Figure 4.17) show that the complex encapsulated in the functionalized micelles maintained its stability, exhibiting a chromatographic profile similar to TBA[Au(cdc)$_2$], with similar retention time, demonstrating that there was no degradation of the complex during the synthesis of the micelles.
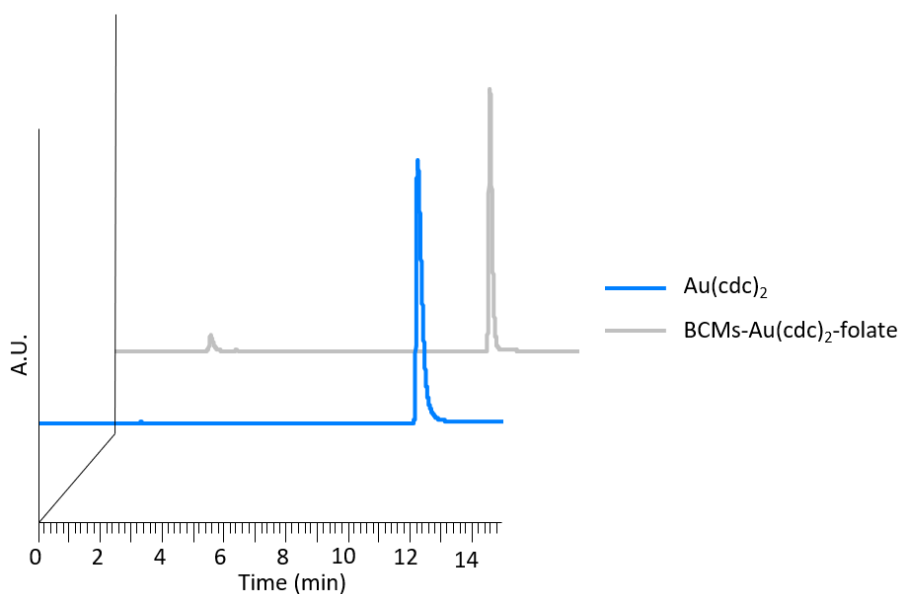
Figure 4.17: HPLC chromatograms of TBA[Au(cdc)$_2$] (R$_t$=12.3 min) and BCMs-Au(cdc)$_2$-folate with UV detection at λ = 303 nm.

4.3 *In vitro* [Au(cdc)$_2$]$^-$ release

The *in vitro* [Au(cdc)$_2$]$^-$ release from BCMs-Au(cdc)$_2$ and BCMs-Au(cdc)$_2$-folate was evaluated by dialysis, using PBS as dialysis medium. This study was performed at 37°C in physiological conditions (pH 7.4) and in acidic conditions (pH 5.5).

For BCMs-Au(cdc)$_2$, the results showed that there was an initial burst release, with 30 to 40% of the cytotoxic drug being released in the first 2 h, followed by a sustained release in the following hours (Figure 4.18) (*vd Appendix B.1* to consult the values). At 8 h of dialysis, 62% of the drug had been released at pH 7.4 and 70% at pH 5.5. This tendency can be observed for the different time points, with the release at acidic pH being approximately 10% higher than at physiological pH. At 24 h incubation time, there was a 96% release from the micelles at pH 7.4, while for the study at pH 5.5 all of the drug had already been released at this time point.
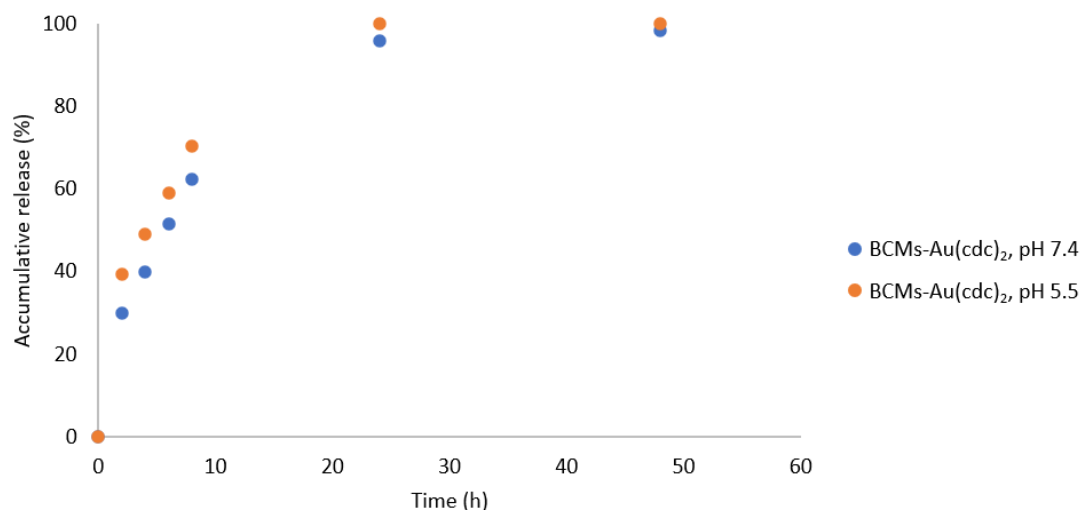
Figure 4.18: *In vitro* $[Au(cdc)_2]^-$ release profile from BCMs-Au(cdc)$_2$ at pH 7.4 and pH 5.5.

For BCMs-Au(cdc)$_2$-folate, Figure 4.19 (*vd Appendix B.2* to consult the values) shows a slightly slower release, compared with BCMs-Au(cdc)$_2$, with only 7 to 13% of the free cytotoxic drug being released in the first 2 h. It can be observed a sustained release throughout the time, with values of 50% at pH 7.4 and 58% at pH 5.5, at 8 h of dialysis. In this case, the difference between the results for pH 7.4 and pH 5.5 is slightly higher, with a difference ranging 20-25% between 4 and 6 h.
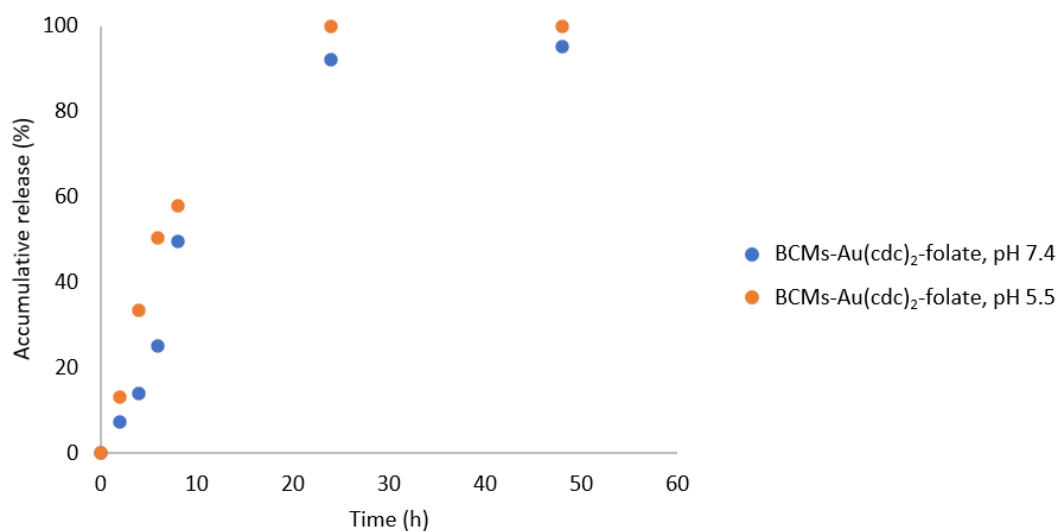
Figure 4.19: *In vitro* $[Au(cdc)_2]^-$ release profile from BCMs-Au(cdc)$_2$-folate at pH 7.4 and pH 5.5.

Although for both micelles, BCMs-Au(cdc)$_2$ and BCMs-Au(cdc)$_2$-folate, it was observed a slight increase in the release of the drug at pH 5.5, compared with pH 7.4, the difference is not statistically significant. However, it should be taken into consideration that the micelles are able to have a full controlled release of the drug.

4.4 Antiproliferative activity

The cytotoxic activity of TBA[Au(cdc)$_2$], BCMs, BCMs-folate, BCMs-Au(cdc)$_2$ and BCMs-Au(cdc)$_2$-folate was evaluated in the cisplatin-sensitive A2780 and OVCAR3 and in the cisplatin-resistant A2780cisR ovarian cancer cell lines, using the colorimetric MTT assay (where MTT = (3-(4,5-dimethylthiazol-2-yl)-2,5-diphenyltetrazolium bromide)). This assay is one of the most widely used methods for assessing cellular viability. It measures the reduction of MTT, a water-soluble yellow tetrazolium dye, into insoluble purple formazan crystals, by mitochondrial dehydrogenases (Figure 4.20). In order to solubilize the formazan crystals, DMSO is usually used, allowing to turn the crystals into a colored solution. After dissolution, the formazan product is analyzed by spectrophotometry (at a wavelength between 500 and 600 nm) and, since the reduction only happens in viable cells, it is possible to establish a relation between the absorbance and the cell metabolic activity, allowing to estimate the level of cytotoxicity [81–83].

3-(4,5-dimethylthiazol-2-yl)-2,5-diphenyltetrazolium bromide (MTT)

(E,Z)-5-(4,5-dimethylthiazol-2-yl)-1,3-diphenyl-formazan (formazan)
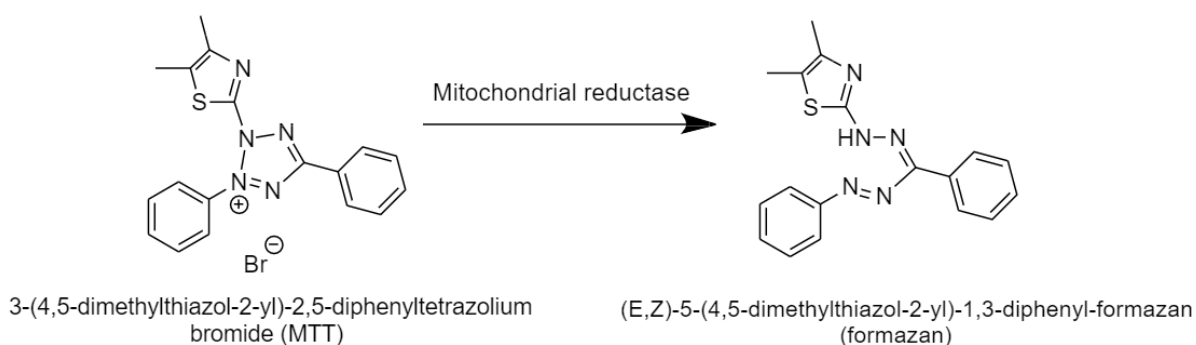
Figure 4.20: Reduction of MTT to formazan. Adapted from [81].

For this study, the antiproliferative effect of the free gold complex TBA[Au(cdc)$_2$] and the loaded micelles (BCMs-Au(cdc)$_2$ and BCMs-Au(cdc)$_2$-folate) was assessed at 48 h incubation time, in the concentration range of 0.01 - 20 μM in the previously mentioned ovarian cancer cell lines. The results obtained showed that the antiproliferative activity depends on the concentration of the gold complex and that the cytotoxicity of [Au(cdc)$_2$]$^-$ is not altered when the complex is encapsulated in the micelles. (Figure 4.21) (*vd Appendix C.1* to consult the values).
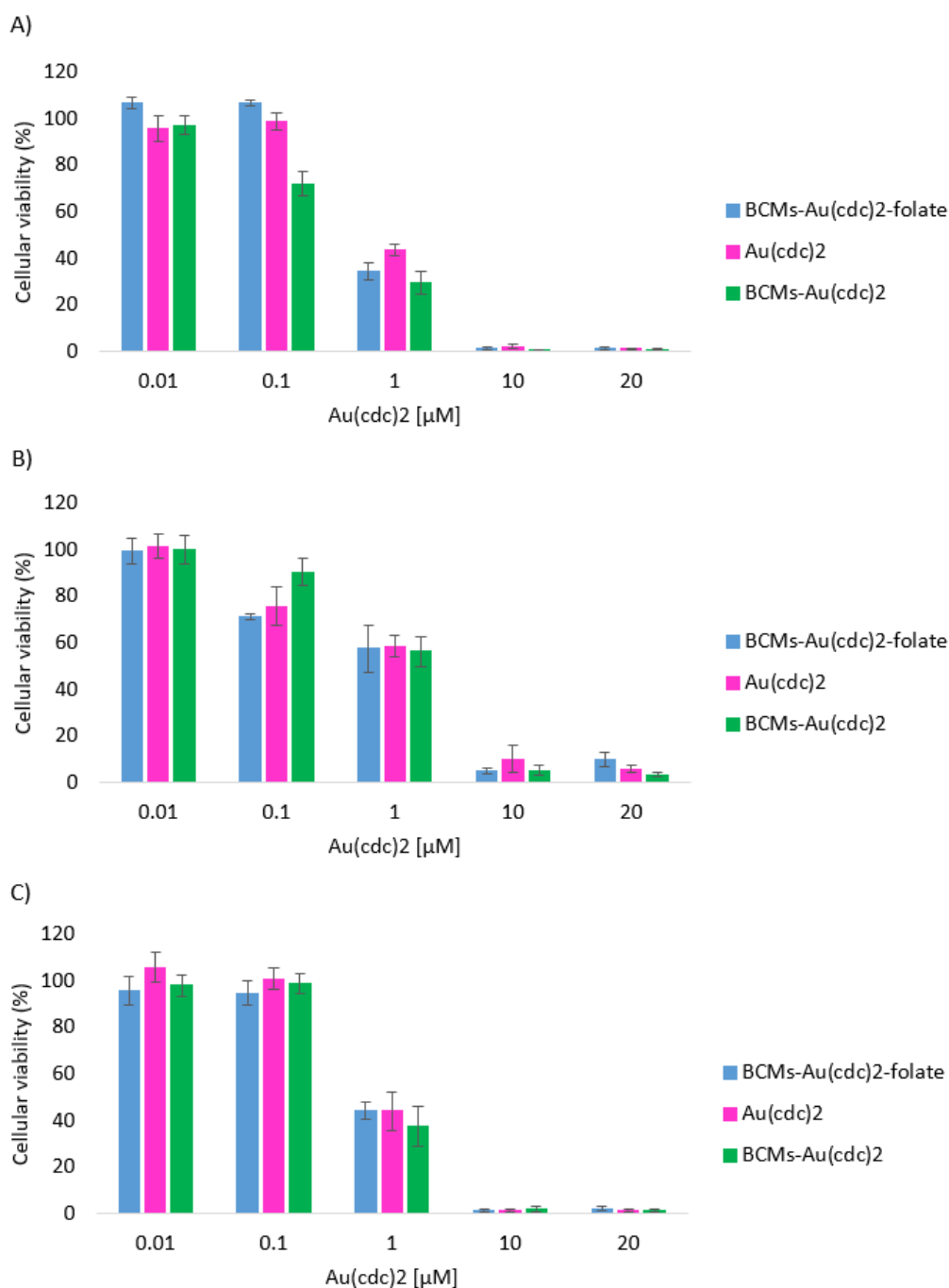
Figure 4.21: Cellular viability studies of BCMs-Au(cdc)$_2$-folate, TBA[Au(cdc)$_2$] and BCMs-Au(cdc)$_2$ after 48 h incubation in the ovarian cancer cell lines: A) A2780; B) A2780cisR and C) OVCAR3. Results shown are the mean±SD of one experiment done with at least three replicates.

Then, the dose response curves were established within the concentration range of 0.01 - 40 μM. The curves obtained for TBA[Au(cdc)$_2$], BCMs-Au(cdc)$_2$ and BCMs-Au(cdc)$_2$-folate were similar, revealing that the presence of folate in the micelles does not alter the cytotoxicity of the complex, contrarily to what would be expected (Figure 4.22).
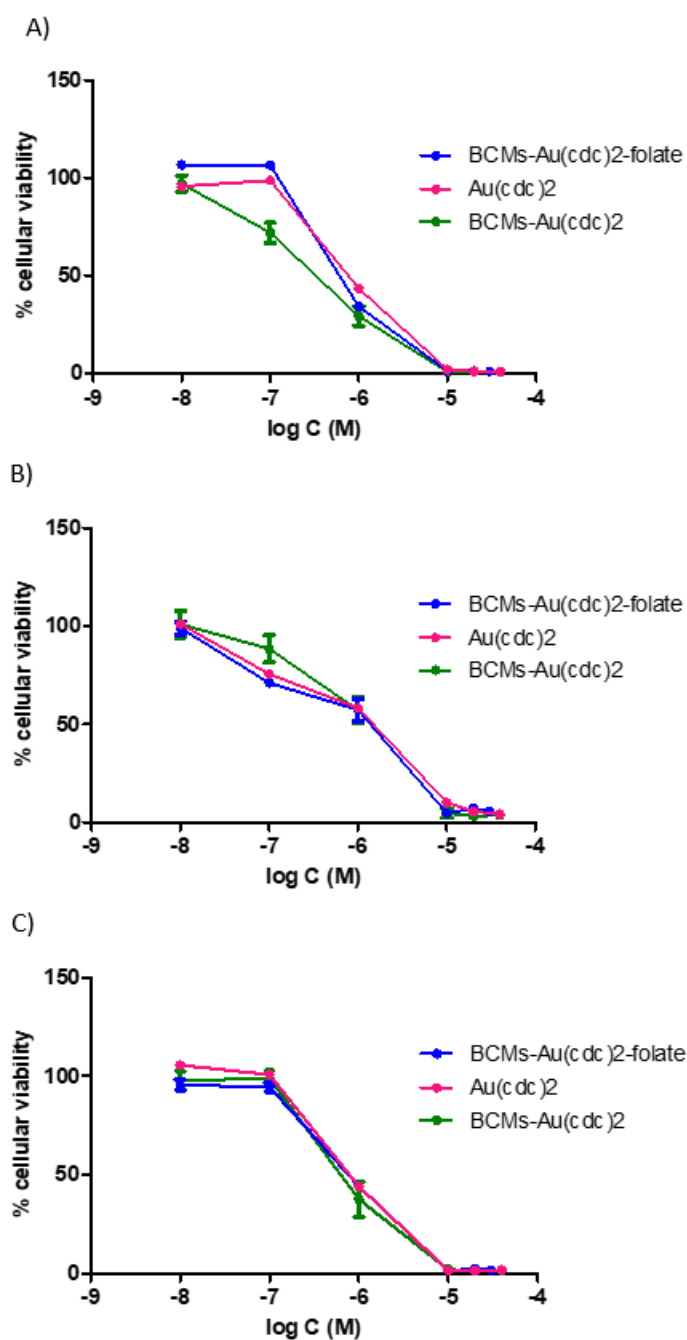
Figure 4.22: Dose-response curves for BCMs-Au(cdc)$_2$-folate, TBA[Au(cdc)$_2$] and BCMs-Au(cdc)$_2$ in the ovarian cancer cell lines: A) A2780; B) A2780cisR and C) OVCAR3. Results shown are the mean±SD of one experiment done with at least three replicates.

The antiproliferative activity of the non-loaded micelles (BCMs and BCMs-folate) was also assessed (Figure 4.23) (*vd Appendix C.2* to consult the values). These micelles did not present significant antiproliferative activity, as expected, demonstrating that the loss of cellular viability is due to the presence of the gold complex.
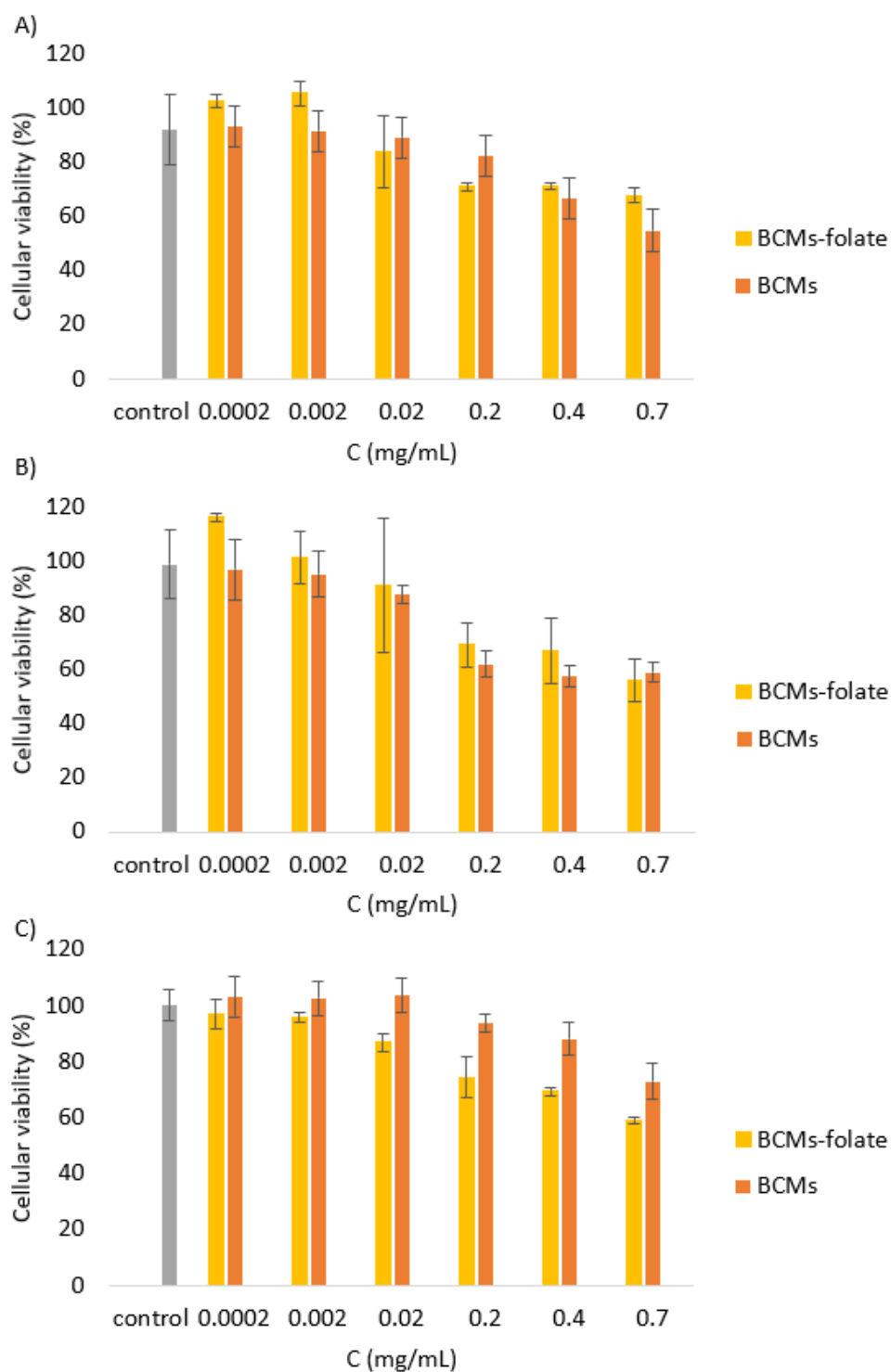
Figure 4.23: Cellular viability studies of BCMs-folate and BCMs after 48 h incubation in the ovarian cancer cell lines: A) A2780; B) A2780cisR and C) OVCAR3. Results shown are the mean±SD of one experiment done with at least three replicates.

The IC_{50} values obtained for both the micelles and the gold complex were similar, demonstrating high cytotoxic activity towards the sensitive and resistant ovarian cancer cell lines (Table 4.4). It is important to note that even for the cisplatin-resistant A2780cisR cell line, the TBA[Au(cdc)$_2$] maintains its cytotoxicity, with IC_{50} values in the same order of magnitude as the ones obtained for the

cisplatin-sensitive A2780 and OVCAR3 cell lines, in accordance with the results previously obtained by Sílvia A. Sousa *et al.* [5], indicating the existence of less cross-resistance, suggesting that this complex could be promising for tackling the problem of drug resistance.

Table 4.4: IC$_{50}$ values (μM) determined after 48 h incubation for TBA[Au(cdc)$_2$], BCMs-Au(cdc)$_2$ and BCMs-Au(cdc)$_2$-folate in the ovarian cancer cell lines A2780, A2780cisR and OVCAR3. Results shown are the mean$\pm$SD of one experiment done with at least three replicates.

	IC$_{50}$ (μM)		
	A2780	A2780cisR	OVCAR3
TBA[Au(cdc)$_2$]	0.82 ± 0.17	1.17 ± 0.38	0.85 ± 0.16
BCMs-Au(cdc)$_2$	0.32 ± 0.04	1.17 ± 0.21	0.70 ± 0.15
BCMs-Au(cdc)$_2$-folate	0.71 ± 0.25	1.00 ± 0.41	0.79 ± 0.13

A summary of the results obtained for the antiproliferative activity of the micelles at 1 μM [Au(cdc)$_2$]$^-$ concentration is presented in Figure 4.24 (*vd Appendix C.3* to consult the values).
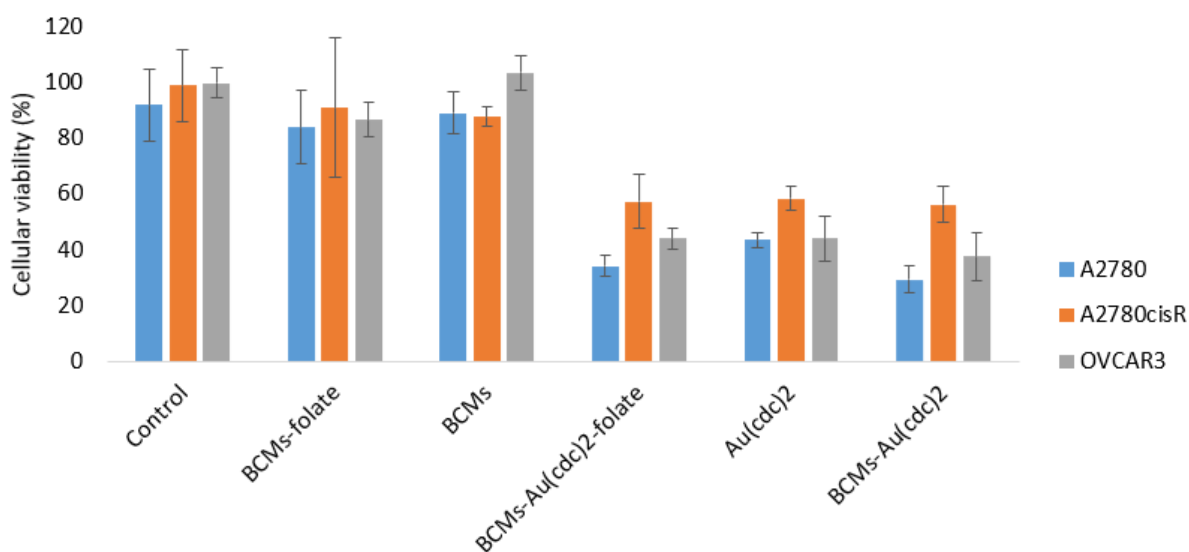
Figure 4.24: Antiproliferative activity study for the micelles in ovarian cancer cell lines A2780, A2780cisR and OVCAR3. For the loaded micelles, [Au(cdc)$_2$]$^-$ concentration was 1 μM and the concentration of the non-loaded micelles was equivalent to that used in the loaded micelles. Results shown are the mean$\pm$SD of one experiment done with at least three replicates.

For the cisplatin-resistant A2780cisR cancer cell line, the antiproliferative effect was slightly lower than for the cisplatin-sensitive cell lines, in accordance to what had been previously reported [5], most likely due to the mechanisms of drug resistance present in these cells. Although the mechanisms underlying platinum resistance are not fully understood, some of these mechanisms are identified, such as reduced drug uptake, enhanced drug efflux and decreased apoptosis due to the increase of DNA

damage repair mechanisms [84, 85]. The promising results obtained for TBA[Au(cdc)$_2$] against the cisplatin-resistant cancer cell line are related with the fact that these novel gold compounds present a different mechanism of action from platinum based compounds, which target DNA, as further explained in Chapter 2.2 [5].

4.5 Radiolabeling with ^{111}In

Indium (In) is a chemical element of Group 13 with the atomic number 49, classified as a post-transition metal. Its eletronic configuration is [Kr] 5s^2 4d^{10} 5p^1 [86]. Indium has isotopes with mass numbers ranging 97 - 135, with only two with known natural abundance, ^{113}In and ^{115}In. The half-life of indium isotopes goes from milliseconds to days [87]. Of all the artificial indium isotopes, ^{111}In is the most used in the development of radiopharmaceuticals.

^{111}In is a readily available γ-emitting radionuclide, which decays by electron capture to stable ^{111}Cd (Figure 4.25), with a half-life of 2.8 days, widely used in nuclear medicine for SPECT imaging. Its relatively long half-life presents an advantage for research, since it allows to perform several studies, both *in vitro* and *in vivo*, for an extended period of time after administration [88]. This characteristic is extremely relevant for the particular case of micelles, since they typically present a prolonged circulation half-life in the blood.

$$^{111}_{49}\text{In}$$

2.8 d

EC ($\approx 100\%$)

7/2 +   120 ps

γ_1 171 keV
(90.7 %)

5/2 +   85 ns

γ_2 245 keV
(94.1 %)

1/2 +   stable

$$^{111}_{48}\text{Cd}$$
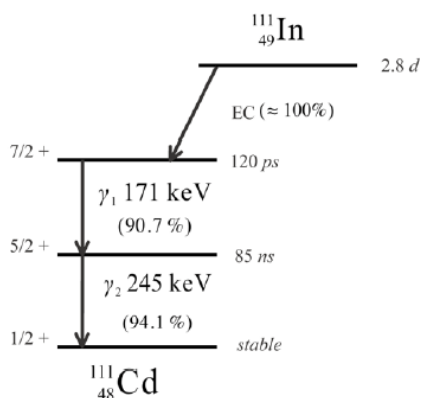
Figure 4.25: Decay scheme of ^{111}In [89]. After electron capture, two gamma rays with 171 and 245 keV energies are emitted.

^{111}In-oxine is widely used in nuclear medicine for labeling of white blood cells, for infection and inflammation scintigraphy, in diseases such as inflammatory bowel disease, neurological infections, endocarditis, lung infections, among others. ^{111}In forms a complex with three 8-hydroxyquinoline ligands when it is in the +3 oxidation state, which can be used to label white blood cells, being able to detect sites of inflammation since, when injected, the labeled white blood cells tend to accumulate in these sites, allowing to identify them through nuclear imaging [90–92].

As explained in Chapter 2.5, for the labeling of nanoparticles, this radionuclide is usually used conjugated with a chelating agent, such as DTPA or DOTA, with promising results, although recent studies have reported the formation of radiocomplexes with lipophilic ligands for the labeling of micelles, with the aim of maintaining the chemical structure of the nanoparticles unaltered and, therefore, maintain the biodistribution and pharmacokinetics of the drugs unaffected by the radiolabeling process.

In this work, the loaded micelles functionalized and non-functionalized with folic acid were labeled with the lipophilic radiocomplex ^{111}In-oxine and *in vitro* stability studies were performed.

4.5.1   Synthesis of ^{111}In-oxine

For the radiolabeling of the micelles with ^{111}In, 8-hydroxyquinoline was first reacted with the radioactive precursor [111]InCl$_3$ to form the neutral hydrophobic complex ^{111}In-oxine. The labeled 8-hydroxyquinoline was then extracted to DCM. The chemical structure of both compounds is shown in Figure 4.26.
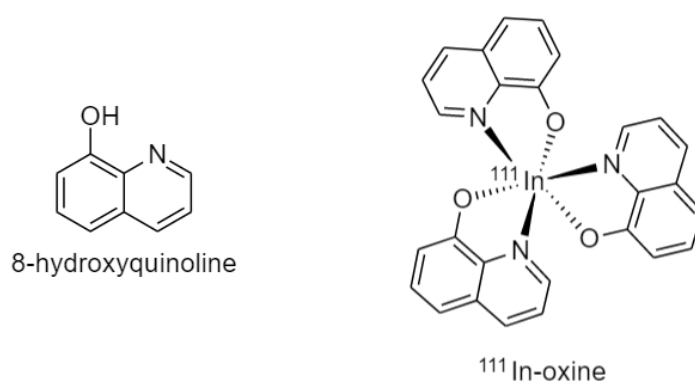
Figure 4.26: Chemical structure of 8-hydroxyquinoline and ^{111}In-oxine.

The radiocomplex was obtained with a radiolabeling efficiency of 72.9%, calculated as the ratio of activity extracted to DCM over the total initial activity of [111]InCl$_3$. The radiochemical purity was evaluated by ITLC-SG, with CHCl$_3$/MeOH (90/10) as eluents. In this chromatographic system [111]InCl$_3$ remains in the application point (Rf = 0) while ^{111}In-oxine migrates with the solvent front (Rf ca 0.9). As can be seen in Figure 4.27 there is no peak at the application point, which indicates that ^{111}In-oxine was obtained with high radiochemical purity (RCP > 99%).
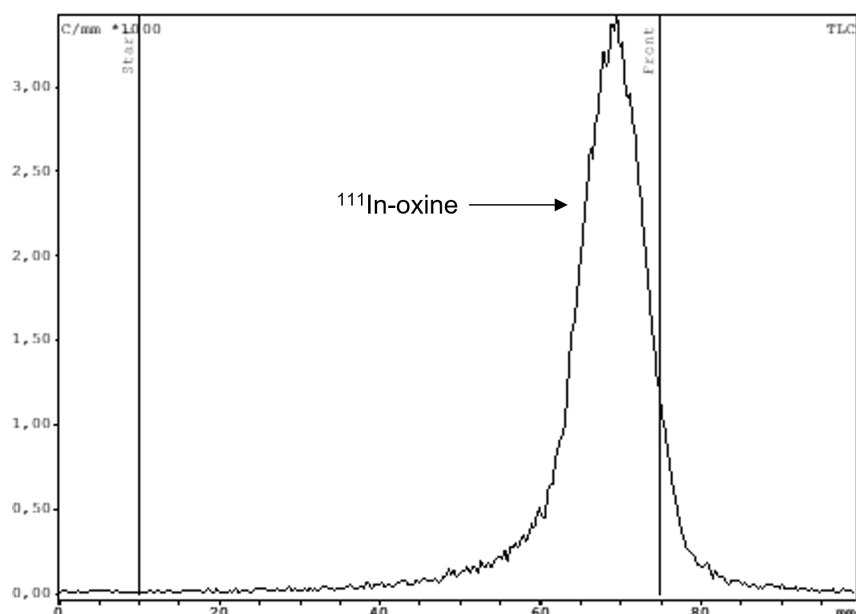
Figure 4.27: Radiochromatogram of ^{111}In-oxine by ITLC-SG using as eluents CHCl$_3$/MeOH (90/10).

4.5.2   Radiolabeling of [Au(cdc)$_2$]$^−$-loaded micelles

After the synthesis of ^{111}In-oxine, the loaded micelles (BCMs-Au(cdc)$_2$) and the loaded micelles functionalized with folic acid (BCMs-Au(cdc)$_2$-folate) were dissolved in PBS, sonicated, mixed with the solution of ^{111}In-oxine and sonicated at 40°C for 20 minutes. Due to the lipophilicity of the radiocomplex, when mixed with the micelles it will be entrapped in the micellar core, forming ^{111}In-BCMs-Au(cdc)$_2$ or ^{111}In-BCMs-Au(cdc)$_2$-folate (Figure 4.28). The radiolabeled micelles were then purified using 10 kDa Amicon centrifugal filters (0.5 mL; MWCO 10 kDa) to remove the non-encapsulated ^{111}In-oxine.
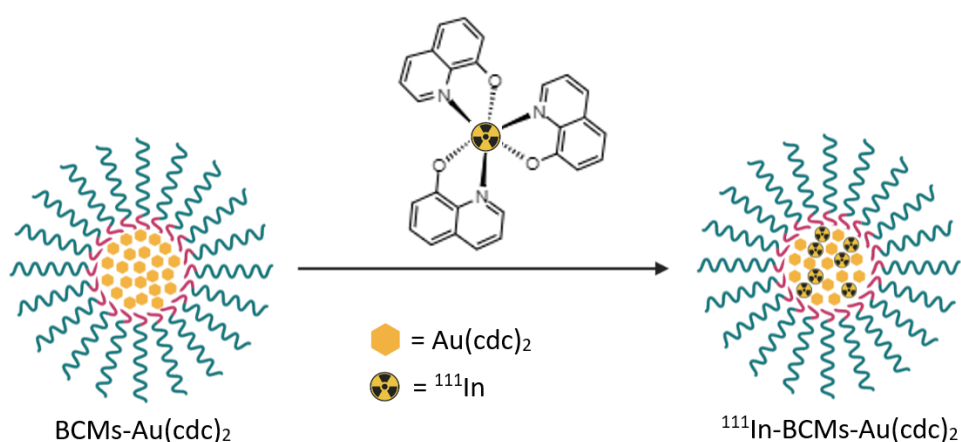
Figure 4.28: Scheme for the synthesis of ^{111}In-labeled micelles.

After purification, the activity in the retentate and in the filtrate was measured and the radiolabeling efficiency was calculated as the percentage of the total activity that was in the retentate, since the radiolabeled micelles are retained in the filter, while the ^{111}In-oxine that was not encapsulated passes to the filtrate. A radiolabeling yield of 91.1% was obtained for ^{111}In-BCMs-Au(cdc)$_2$ and of 90.4% for ^{111}In-BCMs-Au(cdc)$_2$-folate, demonstrating that the presence of folic acid in the shell of the micelles does not alter the radiolabeling efficiency. Although this radiolabeling technique is still not widely used, with the radiolabeling of the shell using a chelating agent being the most common technique, the labeling yield obtained is in accordance with what was observed by Fuente *et al.* (2019) [12] for HPMA-LMA block copolymer micelles. On the other hand, a much lower yield was obtained by Laan *et al.* (2016) [13] (radiolabeling efficiency of 30%), however, in this case, the lipophilic ligand used was tropolone.

4.6 *In vitro* stability studies

The *in vitro* stability of the ^{111}In-BCMs-Au(cdc)$_2$ and ^{111}In-BCMs-Au(cdc)$_2$-folate was evaluated in PBS pH 7.4 and in cell culture media RPMI at 37°C up to 72 h using Amicon centrifugal filters. At different time points, the filters were centrifuged and the filtered was collected. The activity in the retentate and in the filtrate was measured, allowing to determine the percentage of radiolabeled micelles at each time point (Figure 4.29) (*vd Appendix D* to consult the values).
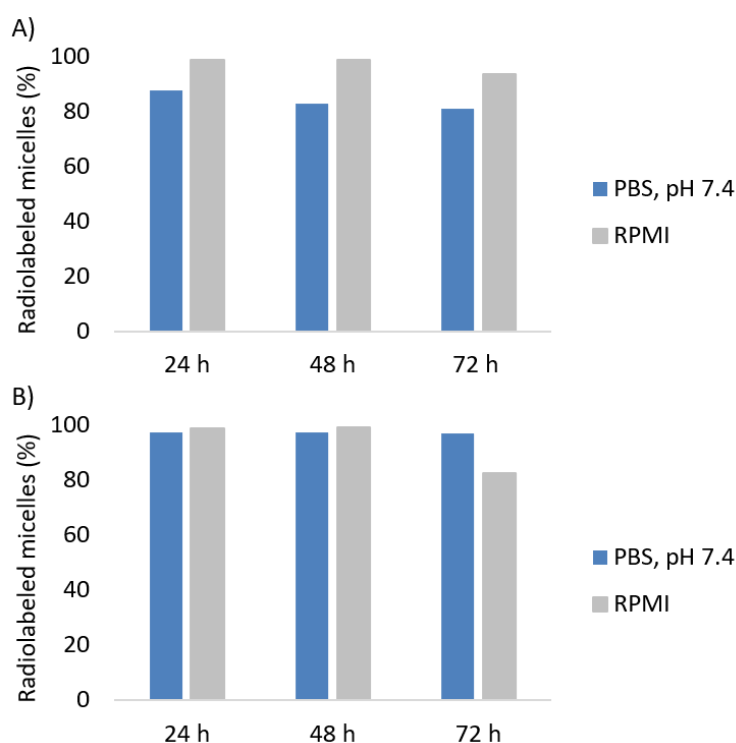
Figure 4.29: *In vitro* stability studies in 0.01 M PBS pH 7.4 and RPMI at 37°C up to 72 h in: A) ^{111}In-BCMs-Au(cdc)$_2$ and B) ^{111}In-BCMs-Au(cdc)$_2$-folate.

The results showed that both radiolabeled micelles were stable under physiological conditions, *i.e.*, at pH 7.4, at 37°C, in both PBS and RPMI, up to 72 h. The ^{111}In-BCMs-Au(cdc)$_2$ presented a slightly higher stability in the cell culture media RPMI, however, this difference is not significant, with the stability in both mediums being higher than 80% in the time points analyzed. The ^{111}In-BCMs-Au(cdc)$_2$-folate presented similar stability in both mediums, with a slight decrease in RPMI at 72 h (83%). Comparing the results obtained for the functionalized and non-functionalized micelles, it is possible to conclude that the functionalization does not affect the stability of the radiolabeled micelles.

The suitable stability of these labeled nanoparticles makes them good candidates for further studies for image-guided drug delivery. Moreover, since the radionuclide complex and the cytotoxic drug are both encapsulated in the core of the micelles, it is expected that the behavior of these two hydrophobic compounds will be similar and, therefore, it is presumed that the non-radiolabeled micelles will also present high stability.

Chapter 5

Conclusions and Future Work

The goal of this thesis was to develop block copolymer micelles functionalized with folic acid, for targeted delivery of a cytotoxic gold complex ($[Au(cdc)_2]^-$) and a radiocomplex (^{111}In-oxine) to ovarian cancer cells.

BCMs carrying $[Au(cdc)_2]^-$ and non-loaded BCMs, functionalized and non-functionalized with folic acid were successfully synthesized, with hydrodynamic diameters below 200 nm and zeta potential values indicating high stability and low tendency to form aggregates, which can optimally contribute to a long circulation half-life *in vivo*. The micelles were obtained with high loading content of $[Au(cdc)_2]^-$, with values of 37.0 $mg_{[Au(cdc)_2]^-}/g_{BCM}$ and 30.0 $mg_{[Au(cdc)_2]^-}/g_{BCM}$, for BCMs-Au(cdc)$_2$ and BCMs-Au(cdc)$_2$-folate, respectively. Moreover, HPLC analysis and UV-Vis spectrophotometry demonstrated that the gold complex maintains its stability after encapsulation in the micelles.

For a better understanding of the behavior of the loaded micelles, *in vitro* release studies were performed, using both functionalized and non-functionalized loaded-BCMs. These studies showed that both micelles present release profiles dependent from the pH of the medium, with a slightly faster release in acidic pH (5.5). Furthermore, the functionalized micelles presented a slightly slower release than the non-functionalized micelles, with a sustained release over time. Although the difference in release rate was not significant between pH 7.4 and 5.5, it should still be taken into account that the micelles were able to fully release the drug in a controlled manner.

The $[Au(cdc)_2]^-$-loaded micelles displayed significant cytotoxic activity towards the cisplatin-sensitive A2780 and OVCAR3 and the cisplatin-resistant A2780cisR ovarian cancer cell lines, comparable to the free gold complex, suggesting that for the same concentration of the complex, a similar therapeutic outcome would be expected. These preliminary studies showed that the cytotoxicity of the functionalized BCMs was similar to that of non-functionalized BCMs, suggesting that the presence of folic acid does not have an influence on the extent of the cytotoxic activity.

The BCMs loaded with $[Au(cdc)_2]^-$ were radiolabeled by entrapping the lipophilic radiocomplex ^{111}In-oxine in the micellar core, with high radiolabeling yield (91.1% for ^{111}In-BCMs-Au(cdc)$_2$ and 90.4%

for ^{111}In-BCMs-Au(cdc)$_2$-folate). Moreover, *in vitro* stability studies showed high stability, with a retention of ^{111}In-oxine above 80% for both micelles in PBS, pH 7.4 and RPMI, up to 72 h at 37°C, suggesting that these platforms could constitute promising strategies for ovarian cancer theranostics.

There are still several studies to be done for a better understanding of the behavior of these micelles and their targeting ability. The cytotoxic activity of the micelles should be evaluated for shorter incubation times, to understand if the differences between the cytotoxicity of the functionalized and non-functionalized micelles become more evident. Furthermore, cellular uptake and biodistribution studies will be performed with the radiolabeled micelles loaded with the complex [Au(cdc)$_2$]$^-$.

Micelles loaded with auranofin could be synthesized and similar studies should be performed, in order to compare the behavior of the recently studied [Au(cdc)$_2$]$^-$ with this well established compound, frequently used as a reference drug for the study of new gold-based drugs.

The micelles functionalized with folic acid could be further explored for targeted therapy of other epithelial tumors overexpressing the folate receptor α, such as breast, kidney and lung tumors. Moreover, the cytotoxicity of the non-functionalized micelles loaded with [Au(cdc)$_2$]$^-$ could be evaluated against other cancer cell lines and decorated with other ligands, to target different receptors.

References

[1] Z. Momenimovahed, A. Tiznobaik, S. Taheri, and H. Salehiniya. Ovarian cancer in the world: epidemiology and risk factors. *International journal of women's health*, 11:287, 2019.

[2] B. S. Doddapaneni, A. M. Al-Fatease, D. A. Rao, and A. W. Alani. Dual-drug loaded micelle for combinatorial therapy targeting hif and mtor signaling pathways for ovarian cancer treatment. *Journal of Controlled Release*, 307:272–281, 2019.

[3] X. Wan, J. J. Beaudoin, N. Vinod, Y. Min, N. Makita, H. Bludau, R. Jordan, A. Wang, M. Sokolsky, and A. V. Kabanov. Co-delivery of paclitaxel and cisplatin in poly (2-oxazoline) polymeric micelles: Implications for drug loading, release, pharmacokinetics and outcome of ovarian and breast cancer treatments. *Biomaterials*, 192:1–14, 2019.

[4] M. J. Mitchell, M. M. Billingsley, R. M. Haley, M. E. Wechsler, N. A. Peppas, and R. Langer. Engineering precision nanoparticles for drug delivery. *Nature Reviews Drug Discovery*, 20(2): 101–124, 2021.

[5] S. A. Sousa, J. H. Leitão, R. A. Silva, D. Belo, I. C. Santos, J. F. Guerreiro, M. Martins, D. Fontinha, M. Prudêncio, M. Almeida, et al. On the path to gold: monoanionic au bisdithiolate complexes with antimicrobial and antitumor activities. *Journal of inorganic biochemistry*, 202:110904, 2020.

[6] K. Kataoka, A. Harada, and Y. Nagasaki. Block copolymer micelles for drug delivery: design, characterization and biological significance. *Advanced drug delivery reviews*, 64:37–48, 2012.

[7] C. Allen, D. Maysinger, and A. Eisenberg. Nano-engineering block copolymer aggregates for drug delivery. *Colloids and Surfaces B: Biointerfaces*, 16(1-4):3–27, 1999.

[8] H. Hatakeyama, H. Akita, and H. Harashima. The polyethyleneglycol dilemma: advantage and disadvantage of pegylation of liposomes for systemic genes and nucleic acids delivery to tumors. *Biological and Pharmaceutical Bulletin*, 36(6):892–899, 2013.

[9] K. R. Kalli, A. L. Oberg, G. L. Keeney, T. J. Christianson, P. S. Low, K. L. Knutson, and L. C. Hartmann. Folate receptor alpha as a tumor target in epithelial ovarian cancer. *Gynecologic oncology*, 108(3):619–626, 2008.

[10] A. R. Hilgenbrink and P. S. Low. Folate receptor-mediated drug targeting: from therapeutics to diagnostics. *Journal of pharmaceutical sciences*, 94(10):2135–2146, 2005.

[11] J. S. Lewis, A. D. Windhorst, and B. M. Zeglis. *Radiopharmaceutical chemistry*. Springer, 2019.

[12] A. de la Fuente, S. Kramer, N. Mohr, S. Pektor, B. Klasen, N. Bausbacher, M. Miederer, R. Zentel, and F. Rösch. 68ga [ga]-, 111in [in]-oxine: a novel strategy of in situ radiolabeling of hpma-based micelles. *American journal of nuclear medicine and molecular imaging*, 9(1):67, 2019.

[13] A. C. Laan, C. Santini, L. Jennings, M. de Jong, M. R. Bernsen, and A. G. Denkova. Radiolabeling polymeric micelles for in vivo evaluation: a novel, fast, and facile method. *EJNMMI research*, 6(1): 1–10, 2016.

[14] K. Kanazaki, K. Sano, A. Makino, F. Yamauchi, A. Takahashi, T. Homma, M. Ono, and H. Saji. Feasibility of poly (ethylene glycol) derivatives as diagnostic drug carriers for tumor imaging. *Journal of Controlled Release*, 226:115–123, 2016.

[15] A. Yoneda, M. E. Lendorf, J. R. Couchman, and H. A. Multhaupt. Breast and ovarian cancers: a survey and possible roles for the cell surface heparan sulfate proteoglycans. *Journal of Histochemistry & Cytochemistry*, 60(1):9–21, 2012.

[16] L. Dong, X. Zhang, L. Cai, F. Zuo, M. Zhao, Q. Wang, S. Zhang, K. Xu, and J. Li. Targeted mri and chemotherapy of ovarian cancer with clinic available nano-drug based nanoprobe. *Biomedicine & Pharmacotherapy*, 130:110585, 2020.

[17] A. R. Carroll, R. L. Coleman, and A. K. Sood. Therapeutic advances in women's cancers. *Frontiers in bioscience (Scholar edition)*, 3:82, 2011.

[18] M. R. Felício, O. N. Silva, S. Gonçalves, N. C. Santos, and O. L. Franco. Peptides with dual antimicrobial and anticancer activities. *Frontiers in chemistry*, 5:5, 2017.

[19] C. Roder and M. J. Thomson. Auranofin: repurposing an old drug for a golden new age. *Drugs in R&D*, 15(1):13–20, 2015.

[20] I. Landini, A. Lapucci, A. Pratesi, L. Massai, C. Napoli, G. Perrone, P. Pinzani, L. Messori, E. Mini, and S. Nobili. Selection and characterization of a human ovarian cancer cell line resistant to auranofin. *Oncotarget*, 8(56):96062, 2017.

[21] U. S. N. L. of Medicine. Clinicaltrials.gov. `https://clinicaltrials.gov/`. (Accessed 23/04/2021).

[22] D. Cirri, T. Schirmeister, E.-J. Seo, T. Efferth, L. Massai, L. Messori, and N. Micale. Antiproliferative properties of a few auranofin-related gold (i) and silver (i) complexes in leukemia cells and their interferences with the ubiquitin proteasome system. *Molecules*, 25(19):4454, 2020.

[23] Z. Yang, G. Jiang, Z. Xu, S. Zhao, and W. Liu. Advances in alkynyl gold complexes for use as potential anticancer agents. *Coordination Chemistry Reviews*, 423:213492, 2020.

[24] T. Zou, C. T. Lum, C.-N. Lok, J.-J. Zhang, and C.-M. Che. Chemical biology of anticancer gold (iii) and gold (i) complexes. *Chemical Society Reviews*, 44(24):8786–8801, 2015.

[25] T. Lammers, W. Hennink, and G. Storm. Tumour-targeted nanomedicines: principles and practice. *British journal of cancer*, 99(3):392–397, 2008.

[26] A. V. Kabanov, E. V. Batrakova, and V. Y. Alakhov. Pluronic® block copolymers as novel polymer therapeutics for drug and gene delivery. *Journal of controlled release*, 82(2-3):189–212, 2002.

[27] R. A. Petros and J. M. DeSimone. Strategies in the design of nanoparticles for therapeutic applications. *Nature reviews Drug discovery*, 9(8):615–627, 2010.

[28] Y. Anraku, A. Kishimura, A. Kobayashi, M. Oba, and K. Kataoka. Size-controlled long-circulating picsome as a ruler to measure critical cut-off disposition size into normal and tumor tissues. *Chemical Communications*, 47(21):6054–6056, 2011.

[29] A. E. Nel, L. Mädler, D. Velegol, T. Xia, E. M. Hoek, P. Somasundaran, F. Klaessig, V. Castranova, and M. Thompson. Understanding biophysicochemical interactions at the nano–bio interface. *Nature materials*, 8(7):543–557, 2009.

[30] J. Fang, H. Nakamura, and H. Maeda. The epr effect: unique features of tumor blood vessels for drug delivery, factors involved, and limitations and augmentation of the effect. *Advanced drug delivery reviews*, 63(3):136–151, 2011.

[31] A. M. Jhaveri and V. P. Torchilin. Multifunctional polymeric micelles for delivery of drugs and sirna. *Frontiers in pharmacology*, 5:77, 2014.

[32] H. Cabral, K. Miyata, K. Osada, and K. Kataoka. Block copolymer micelles in nanomedicine applications. *Chemical reviews*, 118(14):6844–6892, 2018.

[33] Y. Bae, S. Fukushima, A. Harada, and K. Kataoka. Design of environment-sensitive supramolecular assemblies for intracellular drug delivery: Polymeric micelles that are responsive to intracellular ph change. *Angewandte Chemie*, 115(38):4788–4791, 2003.

[34] T. M. Allen. Ligand-targeted therapeutics in anticancer therapy. *Nature Reviews Cancer*, 2(10): 750–763, 2002.

[35] A. J. ten Tije, J. Verweij, W. J. Loos, and A. Sparreboom. Pharmacological effects of formulation vehicles: implications for cancer chemotherapy. *Clin Pharmacokinet*, 42(7):665–685, 2003.

[36] M. L. Adams, A. Lavasanifar, and G. S. Kwon. Amphiphilic block copolymers for drug delivery. *Journal of pharmaceutical sciences*, 92(7):1343–1355, 2003.

[37] M. Yokoyama. Clinical applications of polymeric micelle carrier systems in chemotherapy and image diagnosis of solid tumors. *Journal of Experimental & Clinical Medicine*, 3(4):151–158, 2011.

[38] A. Abuchowski, J. R. McCoy, N. C. Palczuk, T. van Es, and F. F. Davis. Effect of covalent attachment of polyethylene glycol on immunogenicity and circulating life of bovine liver catalase. *Journal of Biological Chemistry*, 252(11):3582–3586, 1977.

[39] D. E. Owens III and N. A. Peppas. Opsonization, biodistribution, and pharmacokinetics of polymeric nanoparticles. *International journal of pharmaceutics*, 307(1):93–102, 2006.

[40] K. Knop, R. Hoogenboom, D. Fischer, and U. S. Schubert. Poly (ethylene glycol) in drug delivery: pros and cons as well as potential alternatives. *Angewandte chemie international edition*, 49(36): 6288–6308, 2010.

[41] A. S. A. Lila, H. Kiwada, and T. Ishida. The accelerated blood clearance (abc) phenomenon: clinical challenge and approaches to manage. *Journal of Controlled Release*, 172(1):38–47, 2013.

[42] S. Mura, J. Nicolas, and P. Couvreur. Stimuli-responsive nanocarriers for drug delivery. *Nature materials*, 12(11):991–1003, 2013.

[43] J. Liu, Y. Huang, A. Kumar, A. Tan, S. Jin, A. Mozhi, and X.-J. Liang. ph-sensitive nano-systems for drug delivery in cancer therapy. *Biotechnology advances*, 32(4):693–710, 2014.

[44] G. Toffoli, C. Cernigoi, A. Russo, A. Gallo, M. Bagnoli, and M. Boiocchi. Overexpression of folate binding protein in ovarian cancers. *International journal of cancer*, 74(2):193–198, 1997.

[45] D. B. Kirpotin, D. C. Drummond, Y. Shao, M. R. Shalaby, K. Hong, U. B. Nielsen, J. D. Marks, C. C. Benz, and J. W. Park. Antibody targeting of long-circulating lipidic nanoparticles does not increase tumor localization but does increase internalization in animal models. *Cancer research*, 66(13): 6732–6740, 2006.

[46] Y. Bae, N. Nishiyama, and K. Kataoka. In vivo antitumor activity of the folate-conjugated ph-sensitive polymeric micelle selectively releasing adriamycin in the intracellular acidic compartments. *Bioconjugate chemistry*, 18(4):1131–1139, 2007.

[47] G. M. Segall, D. A. Pryma, and J. R. Fair. A bright future for nuclear medicine. *Journal of the American College of rRadiology: JACR*, 16(4 Pt A):531, 2019.

[48] S. Jurisson, D. Berning, W. Jia, and D. Ma. Coordination compounds in nuclear medicine. *Chemical Reviews*, 93(3):1137–1156, 1993.

[49] S. Juergens, W. A. Herrmann, and F. E. Kuehn. Rhenium and technetium based radiopharmaceuticals: Development and recent advances. *Journal of Organometallic Chemistry*, 751:83–89, 2014.

[50] S. Adak, R. Bhalla, K. Vijaya Raj, S. Mandal, R. Pickett, and S. Luthra. Radiotracers for spect imaging: current scenario and future prospects. 2012.

[51] S. S. Gambhir. Molecular imaging of cancer with positron emission tomography. *Nature Reviews Cancer*, 2(9):683–693, 2002.

[52] I. Velikyan. Radionuclides for imaging and therapy in oncology. In *Cancer Theranostics*, pages 285–325. Elsevier, 2014.

[53] C.-H. Yeong, M.-h. Cheng, and K.-H. Ng. Therapeutic radionuclides in nuclear medicine: current and future prospects. *Journal of Zhejiang University SCIENCE B*, 15(10):845–863, 2014.

[54] A. Yordanova, E. Eppard, S. Kürpig, R. A. Bundschuh, S. Schönberger, M. Gonzalez-Carmona, G. Feldmann, H. Ahmadzadehfar, and M. Essler. Theranostics in nuclear medicine practice. *OncoTargets and therapy*, 10:4821, 2017.

[55] J. Strosberg, G. El-Haddad, E. Wolin, A. Hendifar, J. Yao, B. Chasen, E. Mittra, P. L. Kunz, M. H. Kulke, H. Jacene, et al. Phase 3 trial of 177lu-dotatate for midgut neuroendocrine tumors. *New England Journal of Medicine*, 376(2):125–135, 2017.

[56] R. P. Baum and H. R. Kulkarni. Theranostics: from molecular imaging using ga-68 labeled tracers and pet/ct to personalized radionuclide therapy-the bad berka experience. *Theranostics*, 2(5):437, 2012.

[57] T. Langbein, W. A. Weber, and M. Eiber. Future of theranostics: an outlook on precision oncology in nuclear medicine. *Journal of Nuclear Medicine*, 60(Supplement 2):13S–19S, 2019.

[58] D. Taïeb, R. J. Hicks, and K. Pacak. Nuclear medicine in cancer theranostics: beyond the target, 2016.

[59] U. Hennrich and K. Kopka. Lutathera: the first fda-and ema-approved radiopharmaceutical for peptide receptor radionuclide therapy. *Pharmaceuticals*, 12(3):114, 2019.

[60] D. of Health and H. Services. NDA Approval. `https://www.accessdata.fda.gov/drugsatfda_docs/appletter/2018/208700Orig1s000ltr.pdf`, . (Accessed 21/05/2021).

[61] D. of Health and H. Services. NDA Approval. `https://www.accessdata.fda.gov/drugsatfda_docs/appletter/2018/208700Orig1s000ltr.pdf`, . (Accessed 21/05/2021).

[62] M. S. Muthu, D. T. Leong, L. Mei, and S.-S. Feng. Nanotheranostics application and further development of nanomedicine strategies for advanced theranostics. *Theranostics*, 4(6):660, 2014.

[63] T. Lammers, S. Aime, W. E. Hennink, G. Storm, and F. Kiessling. Theranostic nanomedicine. *Accounts of chemical research*, 44(10):1029–1038, 2011.

[64] P. Chandrasekharan, D. Maity, C. X. Yong, K.-H. Chuang, J. Ding, and S.-S. Feng. Vitamin e (d-alpha-tocopheryl-co-poly (ethylene glycol) 1000 succinate) micelles-superparamagnetic iron oxide nanoparticles for enhanced thermotherapy and mri. *Biomaterials*, 32(24):5663–5672, 2011.

[65] R. Kumar, A. Kulkarni, D. K. Nagesha, and S. Sridhar. In vitro evaluation of theranostic polymeric micelles for imaging and drug delivery in cancer. *Theranostics*, 2(7):714, 2012.

[66] T.-J. Wu, H.-Y. Chiu, J. Yu, M. P. Cautela, B. Sarmento, J. das Neves, C. Catala, N. Pazos-Perez, L. Guerrini, R. A. Alvarez-Puebla, et al. Nanotechnologies for early diagnosis, in situ disease monitoring, and prevention. In *Nanotechnologies in preventive and regenerative medicine*, pages 1–92. Elsevier, 2018.

[67] B. Hoang, R. M. Reilly, and C. Allen. Block copolymer micelles target auger electron radiotherapy to the nucleus of her2-positive breast cancer cells. *Biomacromolecules*, 13(2):455–465, 2012.

[68] E. Ribeiro, I. Alho, F. Marques, L. Gano, I. Correia, J. D. Correia, S. Casimiro, L. Costa, I. Santos, and C. Fernandes. Radiolabeled block copolymer micelles for image-guided drug delivery. *International journal of pharmaceutics*, 515(1-2):692–701, 2016.

[69] T. F. Scientific. Fisher Scientific. `https://www.fishersci.pt/shop/products/centrifuge-5425-16/15851645`. (Accessed 02/06/2021).

[70] M. Millipore. Merck. `https://www.merckmillipore.com/PT/en/product/Amicon-Ultra-0.5mL-Centrifugal-Filters-for-DNA-and-Protein-Purification-and-Concentration,MM_NF-C82301?ReferrerURL=https%3A%2F%2Fwww.google.com%2F`. (Accessed 02/06/2021).

[71] J. Zhao, C. Wu, J. Abbruzzese, R. F. Hwang, and C. Li. Cyclopamine-loaded core-cross-linked polymeric micelles enhance radiation response in pancreatic cancer and pancreatic stellate cells. *Molecular pharmaceutics*, 12(6):2093–2100, 2015.

[72] V. R. Lincha, J. Zhao, X. Wen, C. Xiong, D. S. Chow, and C. Li. A polymeric micellar drug delivery system developed through a design of experiment approach improves pancreatic tumor accumulation of calcipotriol and paclitaxel. *International journal of pharmaceutics*, 601:120523, 2021.

[73] M. J. Welch and C. S. Redvanly. *Handbook of radiopharmaceuticals: radiochemistry and applications*. John Wiley & Sons, 2003.

[74] H. Danafar, S. Davaran, K. Rostamizadeh, H. Valizadeh, and M. Hamidi. Biodegradable m-peg/pcl core-shell micelles: preparation and characterization as a sustained release formulation for curcumin. *Advanced pharmaceutical bulletin*, 4(Suppl 2):501, 2014.

[75] M. Danaei, M. Dehghankhold, S. Ataei, F. Hasanzadeh Davarani, R. Javanmard, A. Dokhani, S. Khorasani, and M. Mozafari. Impact of particle size and polydispersity index on the clinical applications of lipidic nanocarrier systems. *Pharmaceutics*, 10(2):57, 2018.

[76] S. Samimi, N. Maghsoudnia, R. B. Eftekhari, and F. Dorkoosh. Lipid-based nanoparticles for drug delivery systems. *Characterization and biology of nanomaterials for drug delivery*, pages 47–76, 2019.

[77] E. Joseph and G. Singhvi. Multifunctional nanocrystals for cancer therapy: a potential nanocarrier. *Nanomaterials for drug delivery and therapy*, pages 91–116, 2019.

[78] S.-L. Kim, H.-J. Jeong, E.-M. Kim, C.-M. Lee, T.-H. Kwon, and M.-H. Sohn. Folate receptor targeted imaging using poly (ethylene glycol)-folate: in vitro and in vivo studies. *Journal of Korean medical science*, 22(3):405–411, 2007.

[79] Y. Peng, J. Huang, H. Xiao, T. Wu, and X. Shuai. Codelivery of temozolomide and sirna with polymeric nanocarrier for effective glioma treatment. *International journal of nanomedicine*, 13: 3467, 2018.

[80] S. Zou, N. Cao, R. Z. Du Cheng, J. Wang, K. Zhu, and X. Shuai. Enhanced apoptosis of ovarian cancer cells via nanocarrier-mediated codelivery of sirna and doxorubicin. *International journal of nanomedicine*, 7:3823, 2012.

[81] V. Kuete, O. Karaosmanoğlu, and H. Sivas. Anticancer activities of african medicinal spices and vegetables. In *Medicinal spices and vegetables from Africa*, pages 271–297. Elsevier, 2017.

[82] V. Patravale, P. Dandekar, and R. Jain. Nanotoxicology: evaluating toxicity potential of drug-nanoparticles. *Nanoparticulate Drug Delivery*, 4:123–155, 2012.

[83] P. Wachsmann and A. Lamprecht. Polymeric nanoparticles for the selective therapy of inflammatory bowel disease. *Methods in enzymology*, 508:377–397, 2012.

[84] M. M. Shahzad, G. Lopez-Berestein, and A. K. Sood. Novel strategies for reversing platinum resistance. *Drug Resistance Updates*, 12(6):148–152, 2009.

[85] P. Vasey. Resistance to chemotherapy in advanced ovarian cancer: mechanisms and current strategies. *British journal of cancer*, 89(3):S23–S28, 2003.

[86] PubChem. `https://pubchem.ncbi.nlm.nih.gov/element/Indium#section=Melting-Point`, . (Accessed 21/10/2021).

[87] Jlab - Science Education. `https://education.jlab.org/itselemental/iso049.html`, . (Accessed 21/10/2021).

[88] D. Psimadas, P. Georgoulias, V. Valotassiou, and G. Loudos. Molecular nanomedicine towards cancer: 111in-labeled nanoparticles. *Journal of pharmaceutical sciences*, 101(7):2271–2280, 2012.

[89] M. Uenomachi, K. Shimazoe, K. Ogane, and H. Takahashi. Simultaneous multi-nuclide imaging via double-photon coincidence method with parallel hole collimators. 2021.

[90] M. Roca, E. F. de Vries, F. Jamar, O. Israel, and A. Signore. Guidelines for the labelling of leucocytes with 111 in-oxine. *European journal of nuclear medicine and molecular imaging*, 37(4):835–841, 2010.

[91] W. Becker, W. Fischbach, M. Jenett, C. Reiners, and W. Börner. 111 in-oxine-labelled white blood cells in the diagnosis and follow-up of crohn's disease. *Klinische Wochenschrift*, 64(3):141–148, 1986.

[92] S. S. Lewis, G. M. Cox, and J. E. Stout. Clinical utility of indium 111–labeled white blood cell scintigraphy for evaluation of suspected infection. In *Open forum infectious diseases*, volume 1, page ofu089. Oxford University Press, 2014.

Communications resulting from the work described

- Joana F. Santos, Francisco Silva, Andreia Sousa, Rafaela A.L. Silva, Dulce Belo, Fernanda Marques, Célia Fernandes. Micelle-encapsulated cytotoxic gold complex for cancer theranostics. Flash Presentation at *Workshop 2021 - Thematic Strand Radiopharmaceutical Sciences and Health Physics* (C^{2}TN/IST).

- Joana F. Santos, Francisco Silva, Andreia Sousa, Rafaela A.L. Silva, Dulce Belo, António Matos, Teresa Pinheiro, Fernanda Marques, Célia Fernandes. Selective gold (III) bisdithiolate-loaded micelles to folate receptors in ovarian cancer theranostics. Poster at *II ASPIC-ASEICA International Meeting - Current Trends of Precision Medicine in Cancer*.

Appendix A

Calibration curve

A.1   Values of concentration vs. absorbance

Table A.1: Values of concentration of $[Au(cdc)_2]^-$ vs. absorbance.

Concentration (mg/mL)	Abs
0.00000	0.00000
0.02000	1.12774
0.01500	0.88075
0.01000	0.57077
0.00750	0.45006
0.00375	0.22656
0.00100	0.05840

A.2 Regression

SUMMARY OUTPUT

Regression Statistics

Multiple R	0.999477337
R Square	0.998954947
Adjusted R Square	0.998745937
Standard Error	0.014894325
Observations	7

ANOVA

	df	SS	MS	F	Significance F
Regression	1	1.060276913	1.060276913	4779.447185	1.19919E-08
Residual	5	0.001109205	0.000221841		
Total	6	1.061386117			

	Coefficients	Standard Error	t Stat	P-value	Lower 95%	Upper 95%	Lower 95.0%	Upper 95.0%
Intercept	0.00853551	0.008770362	0.973222043	0.375140595	-0.014009424	0.031080444	-0.014009424	0.031080444
X Variable 1	56.84779557	0.822289595	69.13354601	1.19919E-08	54.73403288	58.96155827	54.73403288	58.96155827

Figure A.1: Regression obtained from Data Analysis in Excel.

Appendix B

Release Studies

B.1 Release study for BCMs-Au(cdc)$_2$

Table B.1: Time (h) vs. values of accumulative release (%) for BCMs-Au(cdc)$_2$.

Time (h)	Accumulative release (%)	
	pH 7.4	pH 5.5
0	0.00	0.00
2	30.10	39.25
4	40.02	49.05
6	51.54	59.04
8	62.44	70.31
24	95.94	100.00
48	98.51	100.00

B.2 Release study for BCMs-Au(cdc)$_2$-folate

Table B.2: Time (h) vs. values of accumulative release (%) for BCMs-Au(cdc)$_2$-folate.

Time (h)	Accumulative release (%)	
	pH 7.4	pH 5.5
0	0.00	0.00
2	7.21	12.94
4	13.90	33.46
6	25.03	50.45
8	49.59	58.02
24	92.16	100.00
48	95.14	100.00

Appendix C

MTT assays

C.1 [Au(cdc)$_2$]$^-$ concentration effect on cell viability

Table C.1: Au(cdc)$_2$ [μM] vs. cellular viability (%) on the A2780 cell line

Au(cdc)$_2$ [μM]	Cellular viability (%)		
	BCMs-Au(cdc)$_2$-folate	Au(cdc)$_2$	BCMs-Au(cdc)$_2$
0.01	106.72 $\pm$ 2.54	97.72 $\pm$ 5.44	97.09 $\pm$ 4.06
0.10	106.53 $\pm$ 1.13	98.64 $\pm$ 3.81	71.90 $\pm$ 5.06
1.00	34.21 $\pm$ 3.66	43.56 $\pm$ 2.73	29.37 $\pm$ 4.97
10.0	1.32 $\pm$ 0.46	2.11 $\pm$ 0.80	0.85 $\pm$ 0.09
20.0	1.27 $\pm$ 0.41	1.08 $\pm$ 0.16	0.94 $\pm$ 0.30

Table C.2: Au(cdc)$_2$ [μM] vs. cellular viability (%) on the A2780cisR cell line

Au(cdc)$_2$ [μM]	Cellular viability (%)		
	BCMs-Au(cdc)$_2$-folate	Au(cdc)$_2$	BCMs-Au(cdc)$_2$
0.01	99.14 $\pm$ 5.55	101.21 $\pm$ 5.24	99.83 $\pm$ 6.12
0.10	71.21 $\pm$ 1.32	75.69 $\pm$ 8.12	90.17 $\pm$ 5.86
1.00	57.41 $\pm$ 9.87	58.45 $\pm$ 4.43	56.21 $\pm$ 6.35
10.0	4.83 $\pm$ 1.09	10.17 $\pm$ 5.57	5.17 $\pm$ 2.21
20.0	9.83 $\pm$ 2.90	5.69 $\pm$ 1.49	3.45 $\pm$ 0.84

Table C.3: Au(cdc)$_2$ [μM] vs. cellular viability (%) on the OVCAR3 cell line

Au(cdc)$_2$ [μM]	Cellular viability (%)		
	BCMs-Au(cdc)$_2$-folate	Au(cdc)$_2$	BCMs-Au(cdc)$_2$
0.01	95.61 $\pm$ 6.27	105.71 $\pm$ 6.43	97.95 $\pm$ 4.69
0.10	94.52 $\pm$ 5.15	100.80 $\pm$ 4.76	98.80 $\pm$ 4.13
1.00	44.12 $\pm$ 3.78	44.01 $\pm$ 8.25	37.50 $\pm$ 8.81
10.0	1.48 $\pm$ 0.52	1.43 $\pm$ 0.52	1.94 $\pm$ 1.39
20.0	2.23 $\pm$ 1.17	1.37 $\pm$ 0.43	1.37 $\pm$ 0.58

C.2 Cellular viability studies for the non-loaded micelles

Table C.4: C (mg/mL) vs. cellular viability (%) on the A2780 cell line

C (mg/mL)	Cellular viability (%)	
	BCMs-folate	BCMs
Control	91.95 $\pm$ 13.16	
0.0002	102.35 $\pm$ 2.41	93.19 $\pm$ 1.71
0.0020	105.32 $\pm$ 4.60	91.45 $\pm$ 3.01
0.0200	83.98 $\pm$ 13.33	89.14 $\pm$ 5.80
0.2000	71.03 $\pm$ 1.45	82.33 $\pm$ 9.96
0.4000	71.03 $\pm$ 1.40	66.59 $\pm$ 8.37
0.7000	67.81 $\pm$ 2.71	54.79 $\pm$ 7.62

Table C.5: C (mg/mL) vs. cellular viability (%) on the A2780cisR cell line

C (mg/mL)	Cellular viability (%)	
	BCMs-folate	BCMs
Control	98.99 $\pm$ 12.86	
0.0002	116.35 $\pm$ 1.50	96.90 $\pm$ 11.27
0.0020	101.59 $\pm$ 9.79	95.34 $\pm$ 8.32
0.0200	91.08 $\pm$ 25.06	87.76 $\pm$ 3.53
0.2000	69.11 $\pm$ 8.08	62.07 $\pm$ 4.70
0.4000	66.88 $\pm$ 12.31	57.41 $\pm$ 3.85
0.7000	56.05 $\pm$ 7.72	58.79 $\pm$ 3.63

Table C.6: C (mg/mL) vs. cellular viability (%) on the OVCAR3 cell line

C (mg/mL)	Cellular viability (%)	
	BCMs-folate	BCMs
Control	100.00	
0.0002	96.81 ± 5.10	103.03 ± 7.20
0.0020	95.74 ± 1.69	102.63 ± 6.21
0.0200	86.72 ± 3.03	103.54 ± 6.29
0.2000	74.39 ± 7.10	93.55 ± 3.36
0.4000	69.20 ± 1.28	87.90 ± 5.85
0.7000	59.04 ± 1.25	72.83 ± 6.26

C.3 Cellular viability studies for Au(cdc)$_2$ concentration of 1μM

Table C.7: Type of micelle vs. cellular viability (%) for Au(cdc)$_2$ concentration of 1μM. The concentration of the non-loaded micelles was equivalent to that used in the loaded micelles.

Micelle	Cellular viability (%)		
	A2780	A2780cisR	OVCAR3
Control	91.95 ± 13.16	98.99 ± 12.86	100.00 ± 5.51
BCMs-folate	83.98 ± 13.33	91.08 ± 25.06	86.72 ± 6.29
BCMs	89.14 ± 7.62	87.76 ± 3.53	103.54 ± 6.29
BCMs-Au(cdc)$_2$-folate	34.21 ± 3.66	57.41 ± 9.87	44.12 ± 3.78
Au(cdc)$_2$	43.56 ± 2.73	58.45 ± 4.43	44.01 ± 8.25
BCMs-Au(cdc)$_2$	29.37 ± 4.97	56.21 ± 6.35	37.50 ± 8.81

Appendix D

Stability Studies

Table D.1: Time (h) vs radiolabeled micelles (%) in ^{111}In-BCMs-Au(cdc)$_2$

Time (h)	Radiolabeled micelles (%)	
	PBS, pH 7.4	RPMI
24	87.8	98.8
48	82.9	98.8
72	81.1	93.9

Table D.2: Time (h) vs radiolabeled micelles (%) in ^{111}In-BCMs-Au(cdc)$_2$-folate

Time (h)	Radiolabeled micelles (%)	
	PBS, pH 7.4	RPMI
24	97.74	99.57
48	97.65	99.15
72	97.05	82.58